

Observations of mesospheric gravity waves generated by geomagnetic activity

Viswanathan Lakshmi Narayanan¹, Corwin James Wright¹, Martin G. Mlynczak², Neil P Hindley¹, Andrew John Kavanagh³, Tracy Moffat-Griffin³, and Phoebe E Noble¹

¹University of Bath

²NASA Langley Research Center

³British Antarctic Survey

October 17, 2023

Abstract

Gravity waves (GWs) play an important role in the dynamics and energetics of the mesosphere. Geomagnetic activity is a known source of GWs in the upper atmosphere. However, how deep the effects of geomagnetic activity induced GWs penetrate into the mesosphere remains an open question. We use temperature measurements from the SABER/TIMED instrument between 2002 - 2018 to study the variations of mesospheric GW activity following intense geomagnetic disturbances identified by AE and Dst indices. By considering several case studies, we show for the first time that the GWs forced by geomagnetic activity can propagate down to about 80 km in the high latitude mesosphere. Only regions above 55° latitudes show a clear response. The fraction of cases in which there is an unambiguous enhancement in GW activity following the onset of geomagnetic disturbance is smaller during summer than other seasons. Only about half of the events show an unambiguous increase in GW activity during non-summer periods and about one quarter of the events in summer show an enhancement in GWs. In addition, we also find that the high latitude mesopause is seen to descend in altitude following onset of geomagnetic activity in the non-summer high latitude region.

Abstract

Gravity waves (GWs) play an important role in the dynamics and energetics of the mesosphere. Geomagnetic activity is a known source of GWs in the upper atmosphere. However, how deep the effects of geomagnetic activity induced GWs penetrate into the mesosphere remains an open question. We use temperature measurements from the SABER/TIMED instrument between 2002 - 2018 to study the variations of mesospheric GW activity following intense geomagnetic disturbances identified by AE and Dst indices. By considering several case studies, we show for the first time that the GWs forced by geomagnetic activity can propagate down to about 80 km in the high latitude mesosphere. Only regions above 55° latitudes show a clear response. The fraction of cases in which there is an unambiguous enhancement in GW activity following the onset of geomagnetic disturbance is smaller during summer than other seasons. Only about half of the events show an unambiguous increase in GW activity during non-summer periods and about one quarter of the events in summer show an enhancement in GWs. In addition, we also find that the high latitude mesopause is seen to descend in altitude following onset of geomagnetic activity in the non-summer high latitude region.

Plain Language Summary

Gravity waves (GWs) exist throughout the atmosphere and are crucial in the dynamics of the middle and upper atmosphere. A variety of processes are known to excite GWs at different altitudes. Above 100 km, space weather induced geomagnetic activity is an important source for the GWs. However, how deep such waves penetrate into the mesosphere, and in what latitude regions their effect is important remains unknown. In this work, we use SABER/TIMED satellite measurements of temperature between 2002 - 2018 to investigate this question. For the first time, we find that the geomagnetic activity forces mesospheric GWs only in the high latitude regions, where enhanced energy deposition occurs along magnetic field lines. Further, these GWs occur only above 80 km, and no unambiguous signature is seen at lower heights. Though damping is expected due to the increasing atmospheric density, this work identifies the altitude and latitude extent for such GWs forced by geomagnetic activity in the mesosphere. Further, there is a significant seasonality in the response such that summer hemisphere shows weakest GW generation due to geomagnetic activity. The mesopause height is also observed to descend during intense geomagnetic disturbances occurring in non-summer periods.

1 Introduction

Atmospheric gravity waves (GWs) are oscillations in the atmosphere spanning a wide range of spatio-temporal scales. Their horizontal sizes range from few 100 m to few 1000 km, with vertical scales of few 100 m to few 10s of km, and time periods vary from about 5 min to several hours, upper limit determined depending on the latitude of observations (Fritts & Alexander, 2003). These waves are forced by different processes in different regions of the atmosphere and propagate away from the source region carrying energy and momentum. They play a crucial role in the vertical coupling of the atmosphere-ionosphere system. The importance of GWs in the upper mesosphere is now well recognized, and the counter-intuitive latitudinal temperature structure of the mesosphere is understood to result from GW driven circulation (Smith, 2012; Blanc et al., 2017). One of the earliest identified sources of upper atmospheric GWs was geomagnetic disturbances (Hunsucker, 1982; Oyama & Watkins, 2012) and it is well known that thermospheric GWs affect the ionosphere and manifest as traveling ionospheric disturbances, though the finer details of this plasma-neutral coupling process remains an active area of research (Zawdie et al., 2022). While the importance of geomagnetic activity as a GW source is well recognized for the thermosphere and E- and F-region ionosphere, the extent to which its dominance penetrates into the middle atmosphere is not properly investigated. It is ex-

66 pected that wave amplitudes will be damped when they propagate downwards due to
67 the exponentially increasing atmospheric density, but it remains unknown how deep ge-
68 omagnetic activity induced GWs occur. Furthermore, prior to this study we do not know
69 if this effect in the middle atmosphere is global or restricted only to the high latitudes.
70 Neither we know about any seasonality in the mesospheric GW response to geomagnetic
71 activity.

72 These aspects remain unknown due to the lack of sufficient data above 70 km at
73 the required spatio-temporal scales. With increasing computational power, modelling of
74 the atmosphere has improved significantly, but most such models focus on the troposphere
75 and stratosphere. Several models are capable of providing physical parameters and chem-
76 ical constituents of the mesosphere, yet GWs are not resolved and tend to be parame-
77 terized. For example the Whole Atmosphere Community Climate Model (WACCM) (Gettelman
78 et al., 2019; Smith et al., 2017), and the Ground-to-topside Atmosphere Ionosphere model
79 for Aeronomy (GAIA) (Jin et al., 2011). Both can include aspects of ionospheric elec-
80 trodynamics to varying degrees. The Thermosphere - Ionosphere - Mesosphere Electro-
81 dynamics - Global Circulation Model (TIME-GCM) is a widely used model in upper at-
82 mosphere - ionosphere studies. It differs from the above mentioned models in that the
83 lower boundary of the model is at stratospheric heights (Roble & Ridley, 1994). Yet, TIME-
84 GCM also uses GW parameterization and suffers from the lack of required spatio tem-
85 poral resolutions to study GW generation from geomagnetic activity. Further, none of
86 these models capture finer variations in the temperature and wind in the mesosphere at
87 the required resolution (Siskind et al., 2019; Harvey et al., 2022; Hindley et al., 2022; Sto-
88 ber et al., 2021; Noble et al., 2022).

89 Ground based measurements are available up to about 100 km but they are typ-
90 ically restricted by geographical location which make it impossible to understand the ef-
91 fects in the global context. An important drawback for ground based radio remote sens-
92 ing of mesospheric neutral wind measurements is that the measured winds are signifi-
93 cantly affected by the ionospheric variability occurring above 90 km (Ramkumar et al.,
94 2002; Reid, 2015). Geomagnetic activity often results in increased contamination from
95 the ionospheric processes at heights above 90 km. Airglow measurements can also pro-
96 vide information about the upper mesosphere, specifically imaging technique is capable
97 of observing different types of waves and instability structures (e.g., Narayanan et al.,
98 2012). However, in the high latitudes, auroral contamination makes imaging of GWs nearly
99 impossible during geomagnetically active times hindering a study of mesospheric GW
100 response using airglow imagers. Therefore, it is important to combine different type of
101 ground based measurements to properly address this problem, for example, combining
102 radar, airglow and lidar measurements. Co-existence of such diverse measurements from
103 single location is extremely rare. Gathering different types of ground based mesospheric
104 measurements from multiple sites to study the mesospheric GW variability correspond-
105 ing to geomagnetic activity has not been accomplished yet.

106 Space based remote sensing from artificial satellites provide an opportunity to mea-
107 sure the atmosphere globally. Many limb sounding and nadir viewing swath measure-
108 ments of atmospheric parameters like temperature and radiance have been used in the
109 past to study GWs (Ern et al., 2004; Alexander et al., 2008; Wright et al., 2011; John
110 & Kumar, 2012; Wright et al., 2016). However, most satellite measurements provide in-
111 formation on neutral atmosphere only to ~ 70 km altitude from the surface. Space based
112 ionospheric measurements are often made in the F-region heights. As a result, the re-
113 gion from 70 - 120 km is unfortunately not well measured with satellite remote sensing.

114 There are some noticeable exceptions to this limited coverage of the 70-120km range
115 like the Wind Imaging Interferometer (WINDII) (Shepherd et al., 2012) and the High
116 Resolution Doppler Imager (HRDI) payloads (McLandress et al., 1996; Fleming et al.,
117 1996) onboard the Upper Atmosphere Research Satellite (UARS) satellite. UARS flew
118 in the early 1990s, but the satellite inclination was low enough that high latitude wind

119 measurements were not available. Further, the measurements had a day-night difference
 120 in the altitude coverage as well. Sounding of the Atmosphere using Broadband Emis-
 121 sion Radiometry (SABER) and TIMED Doppler Interferometer (TIDI) are the payloads
 122 designed to measure temperature and winds, respectively, and flown onboard Thermo-
 123 sphere - Ionosphere - Mesosphere Energetics and Dynamics (TIMED) satellite (Remsberg
 124 et al., 2008; Mertens et al., 2009; Wu & Ridley, 2023). SABER measures temperature
 125 and some minor constituents. TIDI measures four separate line of sight winds and it ap-
 126 pears to have problems in getting proper vector wind estimates continuously (Wu & Ri-
 127 dley, 2023). The Solar Occultation For Ice Experiment (SOFIE) onboard Aeronomy of
 128 Ice in the Mesosphere (AIM) satellite measures temperatures but only during sunrise and
 129 sunset hours of each orbit leaving only ~ 30 profiles at different locations in a day (Gordley
 130 et al., 2009). Recently, the Ionospheric CONnection explorer (ICON) mission had the
 131 Michelson Interferometer for Global High-resolution Thermospheric Imaging (MIGHTI)
 132 payload capable of measuring neutral winds but the satellite is of a low inclination or-
 133 bit not covering middle and higher latitude regions (Harding et al., 2017). Among these,
 134 SABER temperatures have been measured continuously from January 2002 with an al-
 135 titude coverage from upper troposphere to 110 km and near-global spatial coverage. There-
 136 fore, SABER is suitable for studying the importance of space weather sources in gen-
 137 erating GWs into the middle atmosphere. The temperatures are retrieved both during
 138 day and night with reliable error estimates upto about 110 km (Remsberg et al., 2008;
 139 García-Comas et al., 2008). Hence we use SABER data for this study and the analysis
 140 method is explained in the next section.

141 This is the first study to investigate mesospheric GWs forced by geomagnetic ac-
 142 tivity in a global context. This is an important component of space weather impacts on
 143 the middle atmosphere. Further, the observational results provided here are expected
 144 to help formulate model improvements for the upper mesospheric region.

145 2 Data Analysis

146 2.1 Event identification

147 Since our aim is to understand the role of geomagnetic activity in the forcing of
 148 mesospheric GWs, we ensure only the strongest events are selected in order to study the
 149 effects unambiguously. We use AE and Dst indices to identify the events. AE index is
 150 widely used to study the auroral activity and substorm occurrences. AE index is derived
 151 from a set of magnetometers in the northern hemispheric auroral region. The Dst index
 152 is derived from a set of low-mid latitude magnetometer stations and mainly indicates the
 153 ring current and its enhancements. Dst index is used to identify the geomagnetic storms.
 154 First, we focused on major geomagnetic storms having minimum Dst ≤ -200 nT and those
 155 extreme events with a high threshold of AE ≥ 1500 nT. This identified 24 events between
 156 2002 and 2018. Once the AE index reaches beyond 1500 nT, we find the time when the
 157 AE index start to rise above 300 nT. We define this time as start of the event. Short pe-
 158 riod fluctuations of AE < 300 nT are allowed if occurring for less than 8 continuous hours,
 159 so that rapid fluctuations before a major event are accounted for.

160 To improve statistics and check that the results from detailed event-based analy-
 161 sis hold for relatively weaker geomagnetic disturbances, we also identified all events with
 162 maximum AE ≥ 1000 nT. The start for such events is taken as the AE index reaching
 163 300 nT and remaining quasi-continuously high. By quasi-continuous, we allow fluctu-
 164 ations below 300 nT but not for ≥ 8 hours. Often the AE indices will fluctuate above 1000
 165 nT a few times during such intense geomagnetic activity periods. We merge such fluc-
 166 tuations into a single event. In this way, 248 events were identified to perform a seasonal
 167 and hemispherical statistics between 2002 and 2018.

168

2.2 SABER/TIMED data analysis

169

170

171

172

173

174

175

176

177

178

179

180

We use temperature measurements from the SABER instrument onboard the TIMED satellite obtained between 2002 and 2018. The instrument measures limb radiances between 1.27 and 16.9 μm in 10 channels from which temperature and other minor species concentrations are retrieved. Detailed description of the instrument and retrievals can be found elsewhere (Esplin et al., 2023). The latitudinal coverage alternates between 83°N – 52°S and 52°N – 83°S every 60 - 63 days, resulting in coverage of high latitudes only in one of the hemispheres at any given time. The SABER scan is designed such that adjacent profiles are separated alternatively by ~ 250 km and ~ 450 km distances along the track at the upper mesospheric tangent heights. The instantaneous field of view of the instrument is ~ 2 km but the retrievals are made at a finer spacing of about 0.4-0.5 km altitude steps. We apply a 2 km smoothing and resample the data at 1 km vertical intervals. Three such successive profiles are shown in Figure 1(a-c).

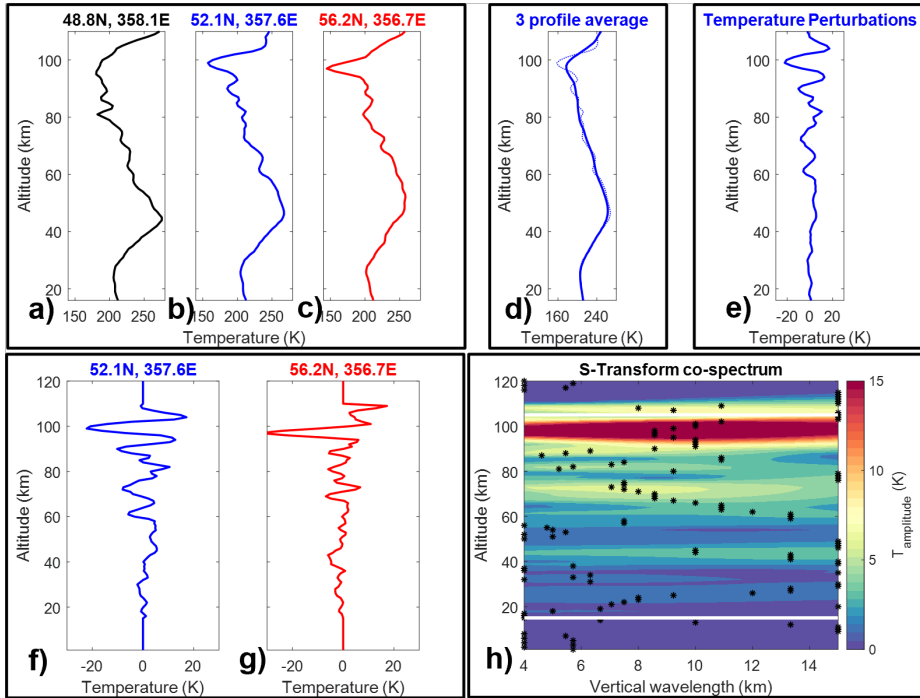


Figure 1. a-c) Three adjacent temperature profiles at 1 km vertical spacing after applying 2 km smoothing (see text for details), d) Thick line shows the 7 km Average of the three profiles shown in panel 'b' which is taken as the background for the center profile (also shown with dotted lines), e) Temperature perturbations obtained after subtracting the background, f-g) Zero padded temperature perturbation profiles, h) Amplitude co-spectra of S-Transform of the profiles. The stars shows the maximum amplitude wave at each altitude which is considered for further calculations of GWPE and MF.

181

182

183

184

185

186

187

In SABER data, each data point in a profile is associated with a latitude, longitude, solar local time (SLT) and universal time (UT). We average these values for each profile between 15 - 110 km heights to represent a mean location and time for the profile. To obtain a background for a particular temperature profile, the adjacent profiles along the satellite track are taken together and a 7 km vertical running average is made on the three profile combination. This background profile is shown in Figure 1(d). The thin dotted line shows the original profile. By subtracting the estimated background pro-

188 file from each profile, we obtain temperature perturbations that are predominantly con-
 189 tributed by GWs (Figure 1(e)). For background estimation, 7 km was selected for the
 190 running average in the vertical after considering a range of step sizes. For smaller step
 191 sizes, many GWs will be included in the background and when it is larger, the mesopause
 192 and any sharp inversion layers will be smoothed out in the background temperature un-
 193 realistically. The latter will generate large perturbation temperatures that are not real
 194 when subtracting the estimated background temperature profile. At the same time, we
 195 note that 7 km coincides with mean scale height. When making background tempera-
 196 ture estimations in this way, the intrinsic assumption is that the background is smooth
 197 over about 700 km in the horizontal, i.e. the average distance covered between 3 pro-
 198 files in the along-track direction.

199 An S-transform analysis is applied to temperature perturbation profiles (Figure 1(e))
 200 following past works (e.g., Stockwell et al., 1996; Alexander et al., 2008; Wright et al.,
 201 2016; Hindley et al., 2019). Hindley et al. (2019) discusses in detail the S-transform cal-
 202 culation that has been adopted herein. The complex output of S-transform of each pro-
 203 file is multiplied by the complex conjugate of the adjacent profile's S-transform to ob-
 204 tain a complex co-spectrum. Figure 1(f-g) shows the adjacent temperature perturbation
 205 profiles zero padded to reduce edge effects resulting in the amplitude co-spectrum shown
 206 in Figure 1(h). The maximum values of the co-spectrum at each altitude is assumed to
 207 represent the dominant wave at that particular altitude. From the magnitude of the com-
 208 plex co-spectrum peak, we obtain the square of the wave amplitude in temperature. By
 209 dividing the phase with the distance between adjacent profiles, we obtain the horizon-
 210 tal wavenumber of the dominant wave (see Alexander et al. (2008); Wright and Gille (2013)
 211 for more details). The corresponding frequency of the co-spectral peak gives the verti-
 212 cal wavenumber. In this way, we obtain an estimate of the amplitude of the dominant
 213 wave perturbation, its vertical and horizontal wavenumbers. Note that we restrict the
 214 vertical scales of the S-transform to 4 - 15 km. The upper limit is aimed at suppressing
 215 long vertical wavelength tidal contributions while the lower limit ensures both the Nyquist
 216 criterion is met and the altitude extent of any instability/turbulence region in the at-
 217 mosphere does not affect the wave results. Because we study geomagnetic disturbances
 218 spanning a few days, the longitudinal coverage is sparse and hence we use zonal aver-
 219 age of the GW parameters in our study.

220 2.3 Gravity wave potential energy and Momentum flux calculations

221 From the estimated wave parameters, gravity wave potential energy (GWPE) and
 222 pseudo-momentum fluxes (MF) are obtained from the following relations. Pseudo-momentum
 223 flux will simply be referred as momentum flux hereafter.

$$E_P = \frac{1}{2} \frac{g^2}{N^2} \left(\frac{T'}{\bar{T}} \right)^2 \quad (1)$$

$$M_f = \frac{\rho \lambda_v}{2 \lambda_h} \frac{g^2}{N^2} \left(\frac{T'}{\bar{T}} \right)^2 = E_P \rho \frac{\lambda_z}{\lambda_h} \quad (2)$$

224 Where, E_P and M_f represents GWPE and MF (the vertical flux of horizontal momen-
 225 tum) respectively (Ern et al., 2004). g and ρ stand for acceleration due to gravity and
 226 density respectively. We used the densities provided by SABER data and account for
 227 the variation of g with height. λ_h and λ_v represent the horizontal and vertical wavelengths
 228 obtained from cospectral analysis. T' is the perturbation temperature and \bar{T} is the back-
 229 ground temperature. We can calculate GWPE using (i) the temperature perturbations
 230 obtained as the amplitude of spectral analysis which correspond to the dominant wave
 231 mode at a height and pair of profiles (the temperature value indicated by the stars in
 232 Figure 1(e) as done in Alexander et al. (2008), for example), and (ii) also using the raw

233 temperature perturbations obtained after subtracting the background temperature es-
 234 timates assuming the contributions from turbulence and tides are negligible compared
 235 to GWs. While the latter assumption is a rudimentary one, the variabilities appear to
 236 be similar in both the potential energy estimates and we prefer to use the ones calcu-
 237 lated from the spectral analysis. The term N in the equation is the buoyancy frequency
 238 calculated from the measured temperature and its gradient as below,

$$N^2 = \frac{g}{T} \left(\frac{dT}{dz} + \frac{g}{C_P} \right) \quad (3)$$

239 where g/C_P is the dry adiabatic lapse rate with C_P , the specific heat at constant pres-
 240 sure taken as $1005 \text{ JKg}^{-1}\text{K}^{-1}$. This is justified because the topmost region considered
 241 in our study is still around the turbopause and the atmosphere remains well mixed. We
 242 divide the momentum flux by atmospheric density (MF/ρ) to result in units of m^2/s^2 ,
 243 which is dimensionally similar to the wind variances due to GWs. This aids in better
 244 visualization of variation with altitude because MF usually given in units of Pa , which
 245 decrease exponentially with height.

246 In the above discussion, the GWs identified are affected by the instrument obser-
 247 vational filter effect, i.e. the sensitivity of a measurement technique to a range of GW
 248 frequencies and wavelengths. No instrument is capable of measuring the whole spectrum
 249 of GWs. The observational filter of SABER is estimated in Figure 9 of Wright et al. (2016).
 250 Because the cospectrum is computed in the satellite's along-track direction, any wavevec-
 251 tor oriented orthogonal to the track will not be observed. For a wave propagating in an
 252 arbitrary direction, the wave vector's projection along the satellite track is identified and
 253 hence the measured horizontal wavenumber is less than the real wavenumber in the hor-
 254 izontal indicating that the measured momentum flux will be less as well. Hence, we are
 255 measuring only a part of the momentum flux from a portion of the GW spectrum that
 256 is restricted by observational filter effect of the instrument. Therefore, we will not fo-
 257 cus on the absolute quantification and the magnitude of the GW momentum fluxes. Rather
 258 we will focus on the relative changes and variations before, during and after the geomag-
 259 netic activity in this work. This realization also enables us to adopt a computationally
 260 efficient way to study the wave variabilities by selecting the dominant wave signature from
 261 the S-Transform instead of selecting waves above a particular threshold or significance
 262 level. This approach is widely used (Alexander et al., 2008; Wright & Gille, 2013; Wright
 263 et al., 2016; Hertzog et al., 2012; McDonald, 2012).

264 To check if there is an unambiguous enhancement following geomagnetic activity,
 265 we calculate GWPE and MF/ρ for 48 hours before and after the start of the event. This
 266 is not based on UT days but is a zonal average of the data for 48 hours before and af-
 267 ter the hour of onset. Note that as described in section 2.1, the start is when the AE reaches
 268 and quasi-continuously stays above 300 nT. The percentage change (C) is evaluated as,

$$C = \frac{(P_{aft} - P_{bef})}{P_{bef}} .100 \quad (4)$$

269 where, P_{bef} and P_{aft} are the 48 hour averages of GWPE or MF/ρ before and after the
 270 onset, respectively. When the mean C between 85 and 100 km altitudes is above +10%
 271 for either GWPE or MF/ρ , it is considered to indicate an unambiguous generation of
 272 GW due to the geomagnetic activity. This threshold of +10% is determined as follows.
 273 Three sets of 500 random dates and times are selected and the 48 hour averages of GWPE
 274 and MF/ρ are calculated and subjected to equation 4. Percentiles of variation are cal-
 275 culated and in all three sets, 10% threshold lies above 85th percentile of the calculated
 276 variations for both GWPE and MF/ρ . It may be noted that the random samplings may
 277 also contain periods of higher geomagnetic activity. No geomagnetic indices are consid-
 278 ered when randomly sampling the start dates. Effectively, 48 hours before and after 500
 279 random samples sum upto 2000 equivalent days resulting in about 5.5 years of randomly

Table 1. Seasons and number of events identified

Seasons	Northern Hemisphere			Southern Hemisphere		
	Duration	No. of. Events		Duration	No. of. Events	
		AE \geq 1500 nT	AE \geq 1000 nT		AE \geq 1500 nT	AE \geq 1000 nT
Winter	22 Oct - 21 Feb	4	34	22 Apr - 21 Aug	7	57
Vernal	22 Feb - 21 Apr	1	14	22 Aug - 21 Oct	2	19
Summer	22 Apr - 21 Aug	4	43	22 Oct - 21 Feb	3	19
Autumn	22 Aug - 21 Oct	1	28	22 Feb - 21 Apr	2	34

280 selected data in each of the sample set. The threshold fixed from such an approach should
 281 be a meaningful one.

282 2.4 Seasonal separation

283 We consider a month on either side of the equinox days as equinoctial periods: Febru-
 284 ary 22 - April 21 and August 22 - October 21. Periods outside these ranges are consid-
 285 ered to represent either summer or winter solstice based on the high latitude hemisphere
 286 covered by the satellite. Table 1 shows the periods considered as summer, winter and
 287 equinoxes in this study along with the number of events identified for different AE thresh-
 288 olds.

289 3 Results

290 3.1 Case Studies

291 3.1.1 Winter observations

292 Figure 2(a) and (b) shows the Dst and AE indices around one of the strongest ge-
 293 omagnetic event of this century, which started on 29 October 2003. The event was a ge-
 294 omagnetic superstorm with a double dip in the Dst index plummeting below -350 nT
 295 and with an AE index crossing 2000 nT. Figure 2(c-f) shows the daily zonal mean of GW
 296 parameters from 90 to 100 km altitude separated into 5 degree latitude bins. GWPE,
 297 Temperature perturbations and MF/ρ (panels (c-e)) show a clear enhancement in wave
 298 activity poleward of $55^\circ N$ during geomagnetic disturbance (see Doy 302 - 306). Verti-
 299 cal wavelengths (Figure 2(f)) show an enhancement during the geomagnetic event around
 300 the same latitude regions where an enhanced wave activity is noticed. Note that these
 301 vertical wavelengths are also zonal averages in 5 degree latitudinal bins. This indicates
 302 that relatively longer vertical wavelength GWs are observed following the storm.

303 Figure 2(g) shows the altitude profiles of GWPE and MF/ρ obtained 48 hours be-
 304 fore (dashed lines) and 48 hours following the storm onset (continuous lines). The re-
 305 gion spanning magnetic inclination of $60^\circ - 90^\circ$ in the Northern hemisphere are aver-
 306 aged herein to obtain the figure since the satellite coverage is in that hemisphere. Av-
 307 eraging with respect to the magnetic inclination values instead of geographic latitude band
 308 is necessary since energy deposition during geomagnetic disturbances directly occur in
 309 the regions with higher magnetic inclinations (and therefore higher magnetic latitudes).
 310 The magnetic inclination values at 100 km altitude are obtained from IGRF 13 model
 311 (Alken et al., 2021). Figure 2(g) shows an unambiguous enhancement of the wave ac-
 312 tivity from about 80 km following the geomagnetic storm. For the first time, this clearly
 313 shows the depth to which dynamic effects of geomagnetic activity penetrates directly.

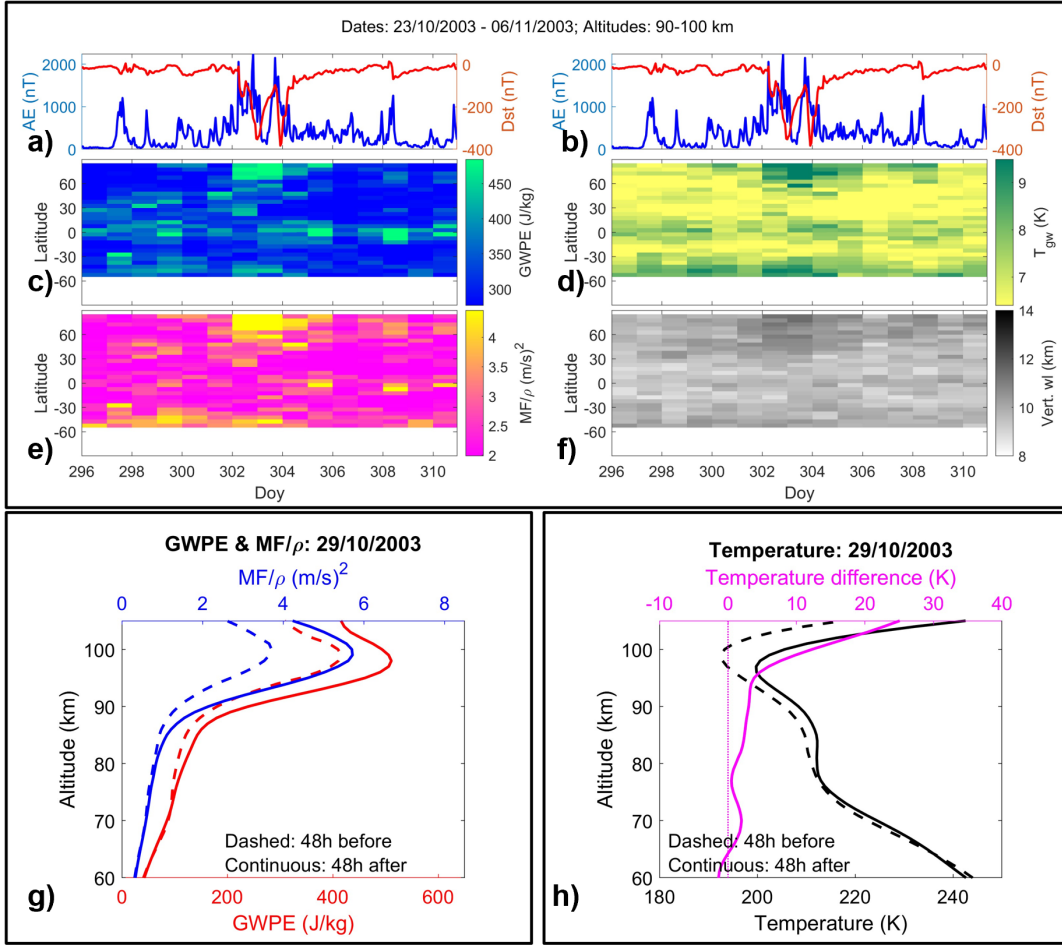


Figure 2. Geomagnetic superstorm of 29 October 2003. a and b) AE and Dst indices, c) GWPE, d) Temperature perturbations before subjecting to spectral analysis, e) MF/ρ , f) Vertical wavelengths. All the parameters in panels c - f are daily longitudinal averages at 5 degree latitude bins. g) Altitude profiles of average GWPE and MF/ρ from 60 – 90° magnetic inclinations in the Northern hemisphere for 48 hours before and after onset of geomagnetic event, and h) Zonal average temperature profiles from 60 – 90° magnetic inclinations for 48 hours before and after the onset of geomagnetic event in black, and the temperature difference in magenta (after - before).

314 Figure 2(h) shows the 48 hour average of temperature profiles before and after the
 315 storm onset plotted in black, calculated for the same geographic region as in Figure 2(g).
 316 This shows the effect of intense geomagnetic activity on the upper mesospheric temper-
 317 ature. There is a heating due to the enhanced geomagnetic activity as can be seen from
 318 the higher temperature values post storm onset. This is better visualized with the mag-
 319 neta curve showing the difference between temperatures after and before the storm onset,
 320 i.e. difference between the continuous and dashed black curves. In addition, the alti-
 321 tude of the mesopause descends as a result of the heating as revealed by the black lines
 322 in Figure 2(h). This is typical for all the events identified except in the summer hemi-
 323 sphere, as will be shown later.

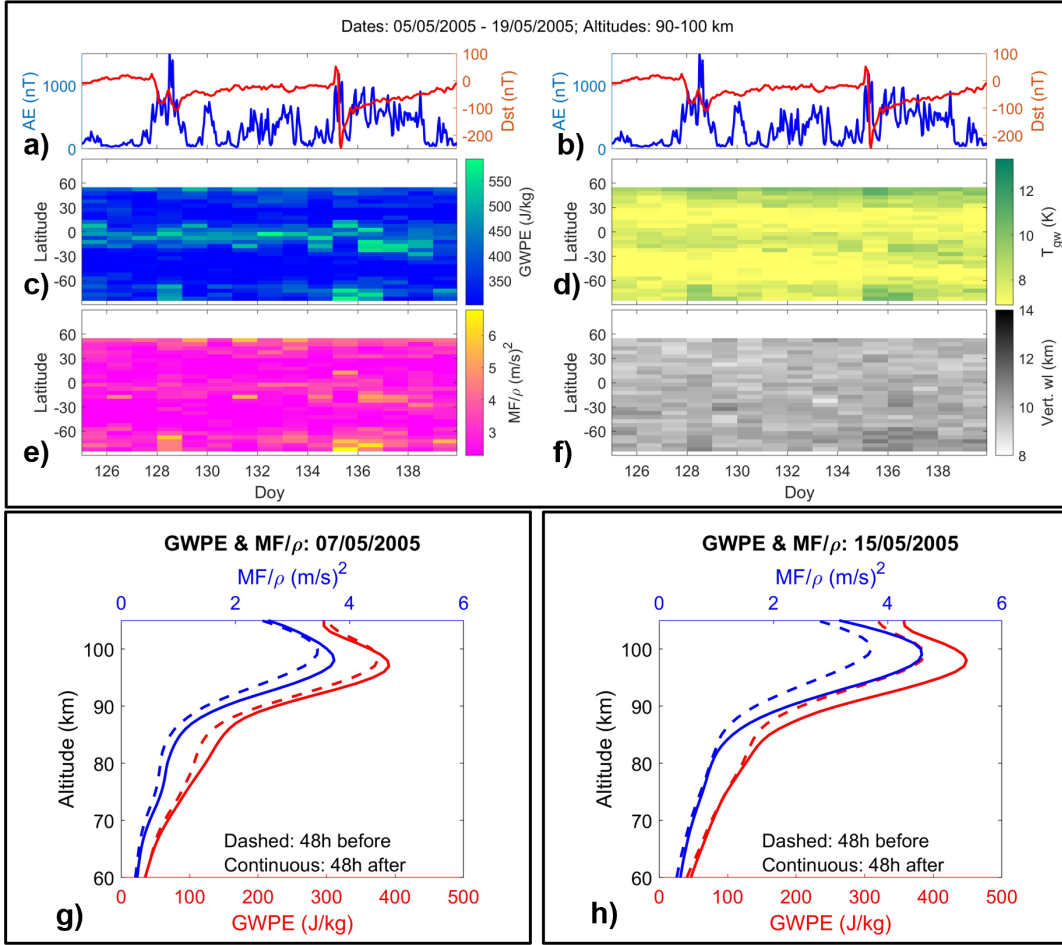


Figure 3. Events of 7 and 15 May 2005. a and b) AE and Dst indices, c) GWPE, d) Temperature perturbations without subjecting to spectral analysis, e) MF/ρ , f) Vertical wavelengths. g and h) Altitude profiles of average GWPE and MF/ρ from $60 - 90^\circ$ magnetic inclinations in the Southern hemisphere for 48 hours before and after the onset respectively for 7 and 15 May 2005.

324 Figure 3 show the results for two events during May 2005. During this period SABER
 325 was covering Southern high latitudes and hence these were observed in winter. The first
 326 event is a compound substorm which started on 7 May and continued until 8 May 2005.
 327 There was only a moderate geomagnetic storm during this period as can be inferred from
 328 the Dst index reaching a minimum close to -100 nT. The second event is that of the major
 329 geomagnetic storm of 15 May 2005 (day of the year (Doy) 135) when the Dst indices
 330 reached below -200 nT (Figure 3(a) and (b)). Though the peak value of AE is higher
 331 during 7-8 May 2005, the event of 15 May 2005 continued for about 3 days and resulted
 332 in one of the severe geomagnetic storms and hence is the stronger prolonged event amongst
 333 the two. From the GWPE, MF/ρ and temperature perturbations (Figure 3(c, e and d)),
 334 it is clear that there is an enhanced wave activity on 8 May 2005 (Doy 128) and 15 and
 335 16 May 2005 (Doy 135 and 136). Similar to the case of 29 October 2003, the vertical wave-
 336 lengths show a coincident enhancement (Figure 3(f)) during both the events in the high
 337 latitudes. Another noticeable feature in Figure 3(c-f) is that the period of 9 - 14 May
 338 2005 is not quiet. Though the AE index has not reached extremely high values of 1000
 339 nT, the period has had significant geomagnetic substorm events and auroral activity. There
 340 are intermittent weaker enhancements in GW activity as well, for example, on days 132

and 133. These observations confirm that intense substorms like that of 7-8 May 2005 also generate GWs into the mesosphere. This implies that the physical processes behind the GW generation are similar for major geomagnetic storms and strong substorms.

Figure 3(g) and (h) respectively show the altitude profiles of average GWPE and MF/ρ for the compound substorm of 7 May 2005 and major geomagnetic storm of 15 May 2005. These profiles are averages between magnetic inclination of -60° – -90° in the Southern Hemisphere. The enhancement in GW activity is larger for the stronger event of 15 May 2005. Similar to the event of 29 October 2003 (Figure 2) and that of 7 November 2004 (not shown), a clear increase in GW activity is seen above 80 km for both these events observed during winter. It appears that the direct penetration of GWs ceases around 80 km and hence geomagnetic activity is an important source only in the upper mesosphere. In addition, the neutral temperature behaviour for these two events (not shown) is similar to that of the 29 October 2003 case (Figure 2(h)) in that the mesopause descended along with higher temperature values post storm onset. Similar descent of mesopause was also noticed during severe storm of 7 November 2004 observed by SABER above the northern high latitudes (not shown).

3.1.2 Summer observations

Figure 4 shows three events in June - July 2005 with onset dates of 12 June (Doy 163), 22 June (Doy 173) and 09 July (Doy 190), respectively. All three events had large AE indices indicating very strong substorm activity, but were only moderate geomagnetic storms with Dst around -100 nT (Figure 4(a) and (b)). Note that generally there is enhanced GW activity at high latitudes during summer irrespective of geomagnetic activity associated enhancements (Figure 4(c-f), above $60^\circ N$). Figure 4(g-i) shows the altitude profiles of the average GWPE and MF/ρ between 60° – 90° inclination angles for the three events. For the first event of 12 June 2005, there is a clear enhancement in the wave activity above ~ 88 km (Figure 4(g)). For the second event beginning on 22 June 2005, there is an enhancement in wave activity only above 94 km (Figure 4(h)). This event does not show a +10% change between 85 - 100 km according to our threshold. Evidently, the magnetic activity levels for 22 June event was weaker compared to that of 12 June 2005 (Figure 4(a-b)).

The third case of 9 July 2005 does not show any enhancement in GW activity (Figures 4(i) and 4(c-e)). However, there is a weak enhancement in average vertical wavelengths for the 9 July 2005 case (Figure 4(f)). It appears as if the geomagnetic activity contributed to some wave generation indicated by vertical wavelength enhancement similar to other cases. Nevertheless, the pre-existing wave activity and its variability during summer masks the contribution from geomagnetic activity. Such a scenario could explain the lack of enhanced wave activity in the averaged wave properties like GWPE and MF/ρ while there is an enhancement in the averaged vertical wavelength. Alternatively, it is likely that the power of pre-existing GW variation was already large during this summer event so that the contribution from geomagnetic activity falls below background levels except in the vertical wavenumber. Figure 4(a-f) has been terminated on 14 July 2005 (Doy 195) right at the end of the multi-night compound substorm event of 9 July 2005 due to a change in SABER latitude coverage.

These events are observed in summer high latitudes where the mesopause occurs below 90 km (Figure 4(j-l)). Note that the mesopause height during summer is not affected following onset of geomagnetic activity contrary to other seasons (black curves). Nevertheless, the extent of heating during summer is comparable to other seasons as seen from the temperature difference profiles after and before the geomagnetic disturbances (magenta curves). Interestingly, the heating during 12 June and 9 July 2005 is comparable in strength but the former shows an enhanced GW forcing below 100 km while the

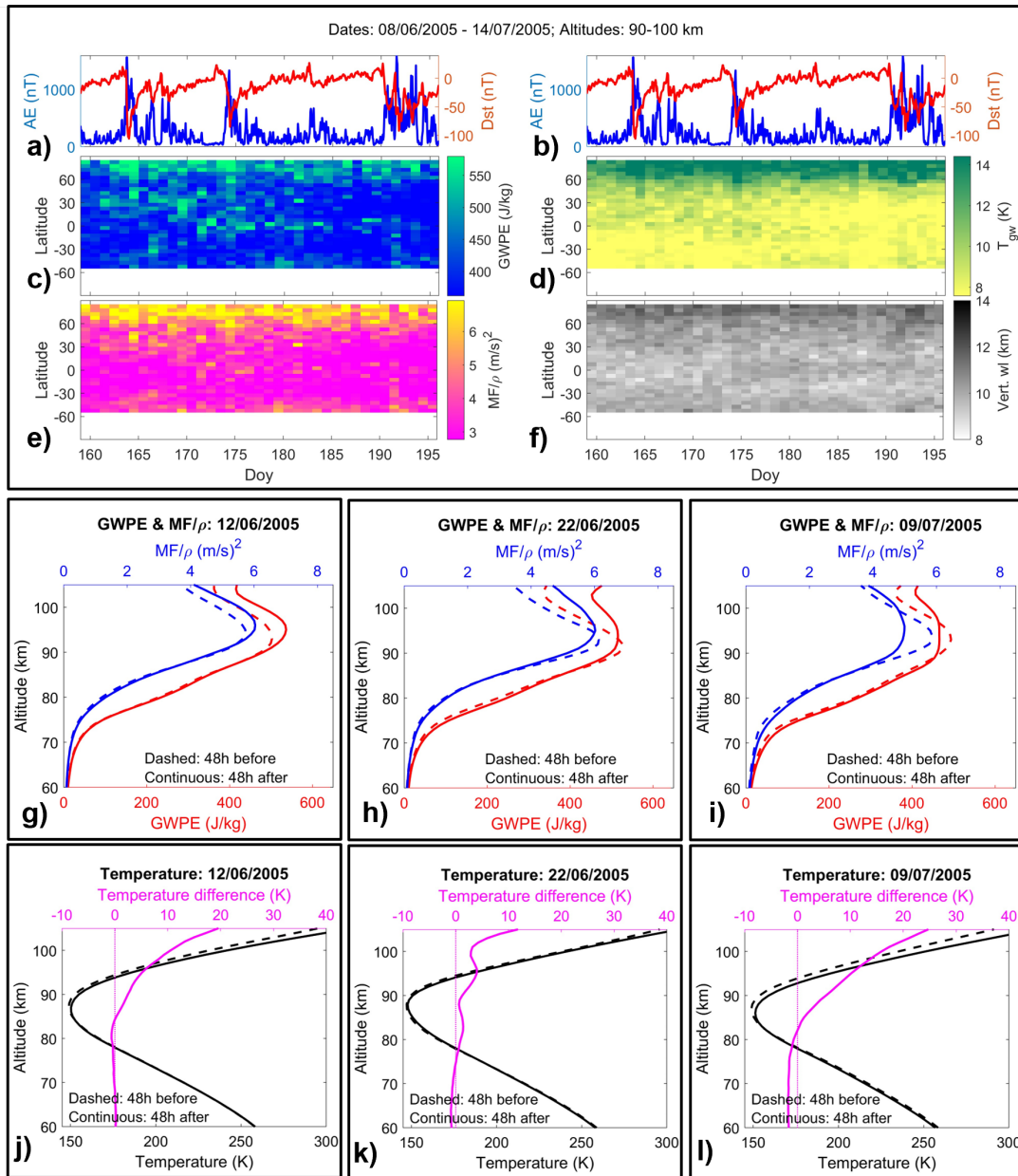


Figure 4. Events of 12 June, 22 June and 9 July 2005. and b) AE and Dst indices, c) GWPE, d) Temperature perturbations without subjecting to spectral analysis, e) MF/ρ , f) Vertical wavelengths.2. g-i) Altitude profiles of zonal average GWPE and MF/ρ 48 hours before and after the geomagnetic disturbances. j-l) Zonal average temperature profiles from 60 – 90° magnetic inclinations for 48 hours before and after the onset of geomagnetic event in black, and the temperature difference post and pre onset in magenta.

391 latter does not. Thus, the summer high latitudes appear to respond in a different man-
 392 ner to the geomagnetic activity as seen above within a span of 30 days.

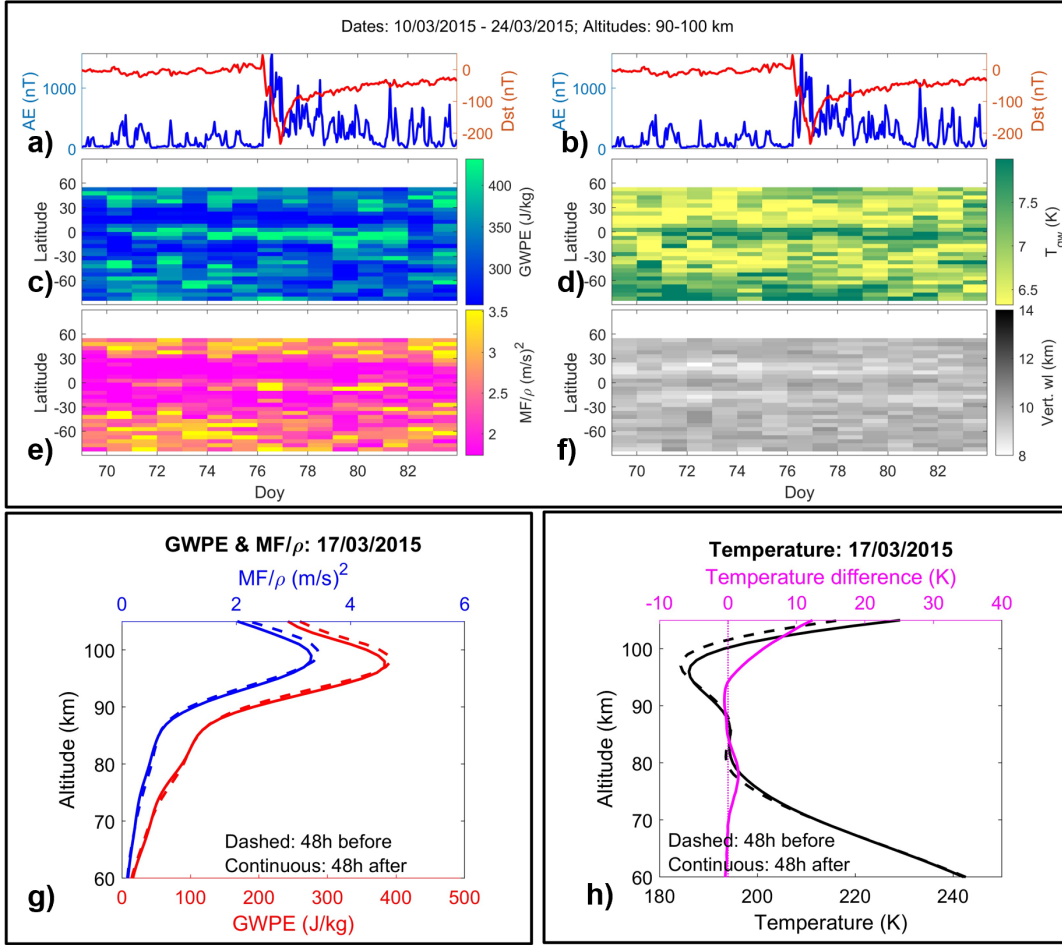


Figure 5. St. Patrick's Day storm of 17 March 2015. Figures are in the same format as that of Figure 2.

3.1.3 Equinoctial observations

Figure 5 shows observations during the St. Patrick's Day storm of 17 March 2015. SABER was measuring Southern high latitudes and thus this event falls under Autumn equinox. This was the strongest geomagnetic storm of solar cycle 24. During this event, the Dst index reached -223 nT and the AE index reached 1570 nT with significantly high values (i.e. above 1000 nT) from 17 to 19 March 2015. However, this event did not lead to a noticeable increase in GW activity as seen from Figure 5(c-f). Figure 5(g) showing altitude profiles of GWPE and MF/ρ before and after the event further confirms lack of enhancement in the GW activity. This is surprising when noticing that even compound substorms have been shown to lead to enhanced GW activity (for example, Figures 3 and 4). At the same time, Figure 5(h) displaying that the average temperature profiles before and after the onset of the event still shows a reduction in the mesopause altitude and heating above 90 km. Nevertheless, no enhancement in GW activity is seen. It is worth noting that there was lack of response to another relatively weaker geomagnetic event on 17 March 2013, which was also observed by SABER over the southern high latitudes (not shown).

On the other hand, another autumn equinox observation during 26 September 2011 shows a noticeable enhancement in GW activity over Northern high latitudes as shown

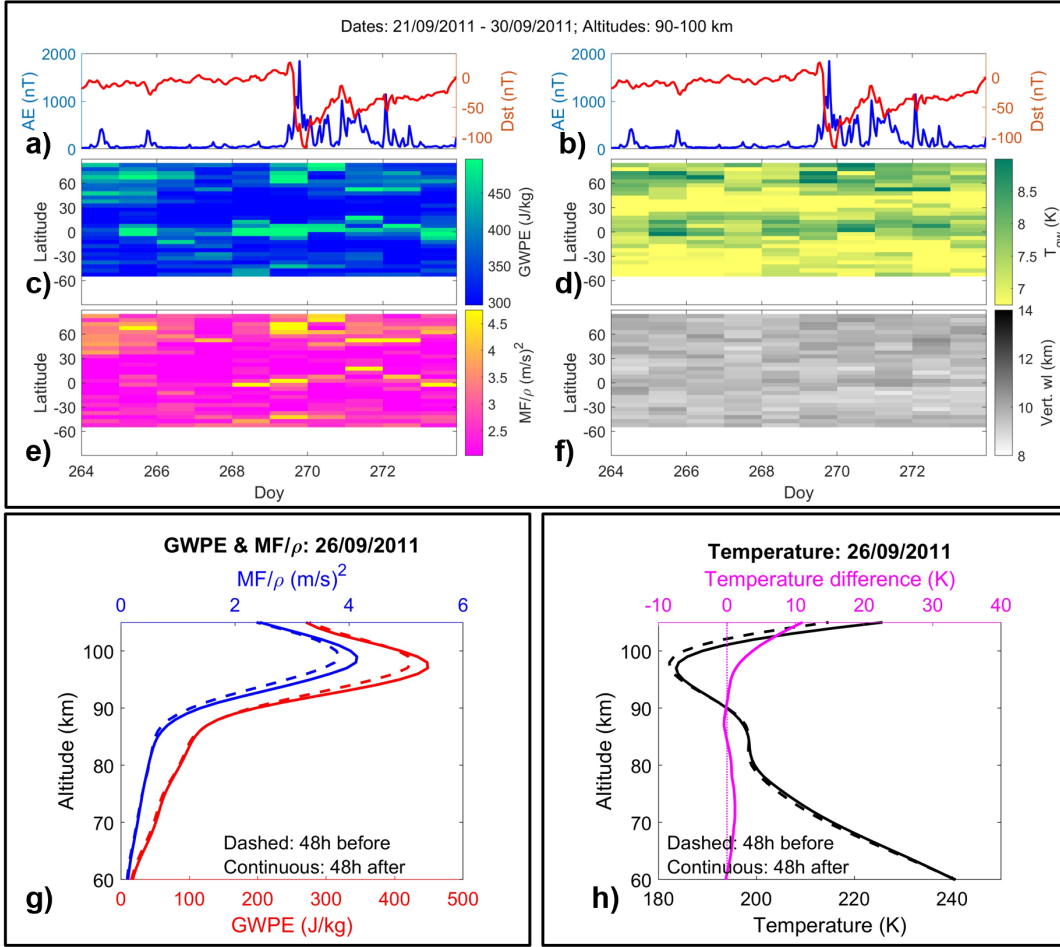


Figure 6. Autumn equinox observation showing an enhancement in GW activity. Figures are in the same format as that of Figure 2.

411 in Figure 6. This event was a compound substorm which co-occurred with a geomag-
 412 netic storm with Dst index of about -100 nT. The St. Patrick's Day storms of 2015 (Fig-
 413 ure 5) and 2013 are more intense geomagnetic events that did not lead to an increase
 414 in GW activity. The 48 hour average temperature profile comparisons before and after
 415 the onset for the event of 26 September 2011 shown in Figure 6(h) indicates similar heat-
 416 ing and a reduction in the mesopause altitude compared to 17 March 2015 event (Fig-
 417 ure 5(h)). This further implies that the GW response does not merely depend on the strength
 418 of heating or the extent of the descent of mesopause. Therefore, other factors like tem-
 419 perature gradient, wind variations and pre-existing wave activity play a role in the ext-
 420 ent of enhancement in the GW activity post onset of a geomagnetic event.

421 Three events occurred during vernal equinox season with $AE \geq 1500$ nT, and two
 422 of them showed a clear enhancement in GW activity following the start of geomagnetic
 423 disturbance. Each hemisphere witnessed one such event (not shown).

424 3.2 Statistics

425 First, we discuss the cases where the maximum AE index is above 1500 nT or min-
 426 imum Dst index below -200 nT from which the individual cases shown in the previous

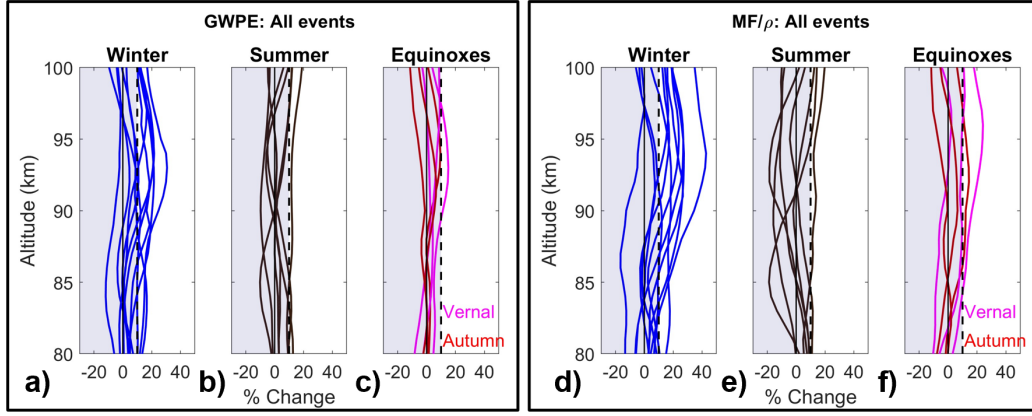


Figure 7. Percentage changes of GWPE for (a) winter, (b) summer and (c) equinoxes, and MF/ρ for (d) winter, (e) summer and (f) equinoxes for the events having threshold values of $AE \geq 1500$ nT or $Dst \leq -200$ nT. The region below +10% is shaded.

427 section are selected. Figure 7(a-c) and (d-f) shows the altitude profiles of percentage changes
 428 of GWPE and MF/ρ , respectively, for all the events selected according to equation 4.
 429 The thin black vertical line indicates 0 and thick dashed black line corresponds to +10%,
 430 our threshold to unambiguously identify a change post onset of geomagnetic activity. The
 431 region below +10% are shaded in Figure 7. Note that most of the winter cases in Fig-
 432 ure 7(a) and (d) show positive excursion beyond 10% threshold in the 80 - 100 km alti-
 433 tude range, while only 1 case in summer show a such a behaviour (Figure 7(b) and (e)).
 434 During equinoxes, 3 out of 6 events showed a positive excursion beyond 10% line for MF/ρ
 435 (Figure 7(f)).

436 In order to increase the number of cases and ensure that the statistics discussed
 437 above hold, we proceed to analyze all events with peak $AE > 1000$ nT. Out of the 253
 438 identified events, 5 occurred around the dates of SABER/TIMED yaw change and hence
 439 cannot be used, leaving 248 events for statistical analysis. For these events we calculate
 440 the percentage changes in GWPE and MF/ρ and define an average percentage change
 441 greater than 10% between 85 and 100 km altitudes as a meaningful change. The results
 442 are shown in Figure 8(a) for both the hemispheres and 8(b) and (c) respectively for the
 443 Northern and Southern hemispheres. Figure 8 shows a clear dip in summer in the re-
 444 sponse, in concurrence with our case studies (Figure 7). The responses are similar be-
 445 tween the hemispheres. Statistically, the GW enhancements during equinoxes appear to
 446 be slightly stronger than those during the winter solstice in the Northern hemisphere than
 447 the Southern hemisphere.

488 4 Discussion

449 In this section, we will consolidate the above observations and discuss the reasons
 450 for the observed seasonality in the GW response to geomagnetic activity. As seen from
 451 examples given in Figure 3, 4 and 6, we note that intense substorm activity plays an im-
 452 portant role in affecting the GW variability. It is known that geomagnetic disturbances
 453 may arise from different drivers such as coronal mass ejections, corotating interaction
 454 regions and high-intensity long-duration continuous AE activity (HILDCAA). We did
 455 not separate the events based on the drivers because all of them produce substorms and
 456 almost all intense geomagnetic storms co-occur with strong substorm events. The en-
 457 hancement in GW activity is always observed only in the high latitude regions, and more
 458 importantly they occur in a transient manner nicely coinciding with the periods of ge-

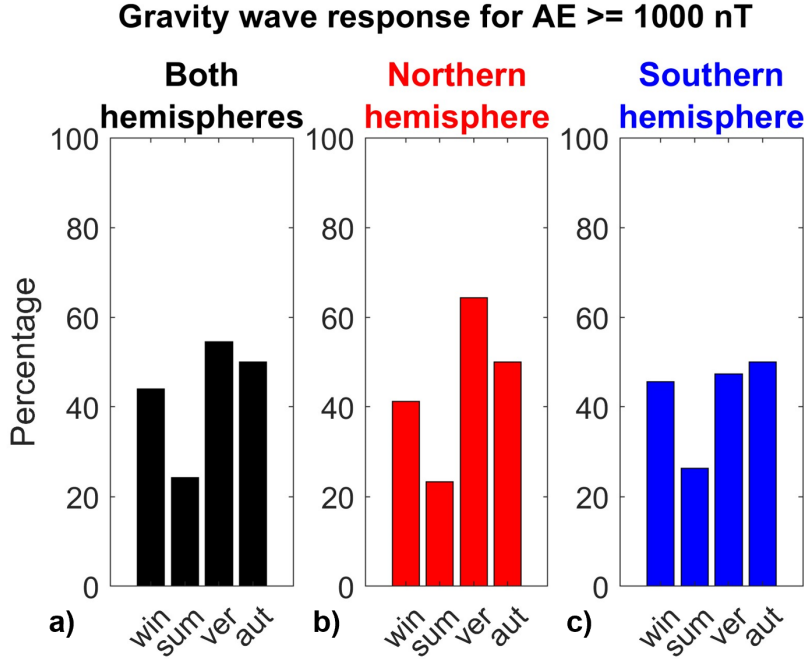


Figure 8. Seasonal and hemispherical response for geomagnetically active events having maximum $AE \geq 1000$ nT .

459 omagnetic disturbances as seen from AE index enhancements (Figures 2 - 6). This in-
 460 dicates that active forcing generates the GWs, i.e. they are not propagating from else-
 461 where. Hence substorm related heating effects appear to be the source for these GWs.

462 Two major GW sources in the high latitude upper atmosphere associated with ge-
 463 omagnetic activity are Joule and particle heating (Oyama & Watkins, 2012). Joule heat-
 464 ing peaks in the region of 120 - 130 km while particle heating peaks at lower altitudes
 465 where the atmospheric density is large enough for frequent collisions. An increase in ver-
 466 tical wavelength coincident with the increased GW activity following geomagnetic dis-
 467 turbances is observed in $\sim 70\%$ of the cases with peak $AE \geq 1500$ nT. This preferen-
 468 tial formation of longer vertical wavelength GWs following geomagnetic activity might
 469 be an indication of the underlying generation mechanism. From the temperature pro-
 470 files shown in Figures 2, 4, 5 and 6, it is seen that heating occurs above 90 km. This im-
 471 plies that particle heating is likely to be the important source responsible for the GWs
 472 observed below 100 km, because heating may occur almost in-situ and immediately above
 473 the region of wave observation. Particle heating may also have a matching vertical scale
 474 length to that of observed vertical wavelengths.

475 The weaker summer response of GW activity to geomagnetic disturbances may be
 476 due to a combination of seasonal variations in wave forcing, temperature structure and
 477 pre-existing GW activity. If Joule heating creates a portion of the observed GWs, the
 478 extent of Joule heating will be lesser in the enhanced ionospheric conductivities of the
 479 sunlit summer high latitudes compared to other seasons. The extent of particle heating
 480 in summer below 100 km is also lesser or of comparable magnitude to the other seasons
 481 - for example, compare Figure 4(j-l) with those of Figures 2(h), 5(h) and 6(h). These in-
 482 dicate that there is at least no excessive Joule or particle heating occurring in the sum-
 483 mer to force significantly larger amounts of GWs than other seasons.

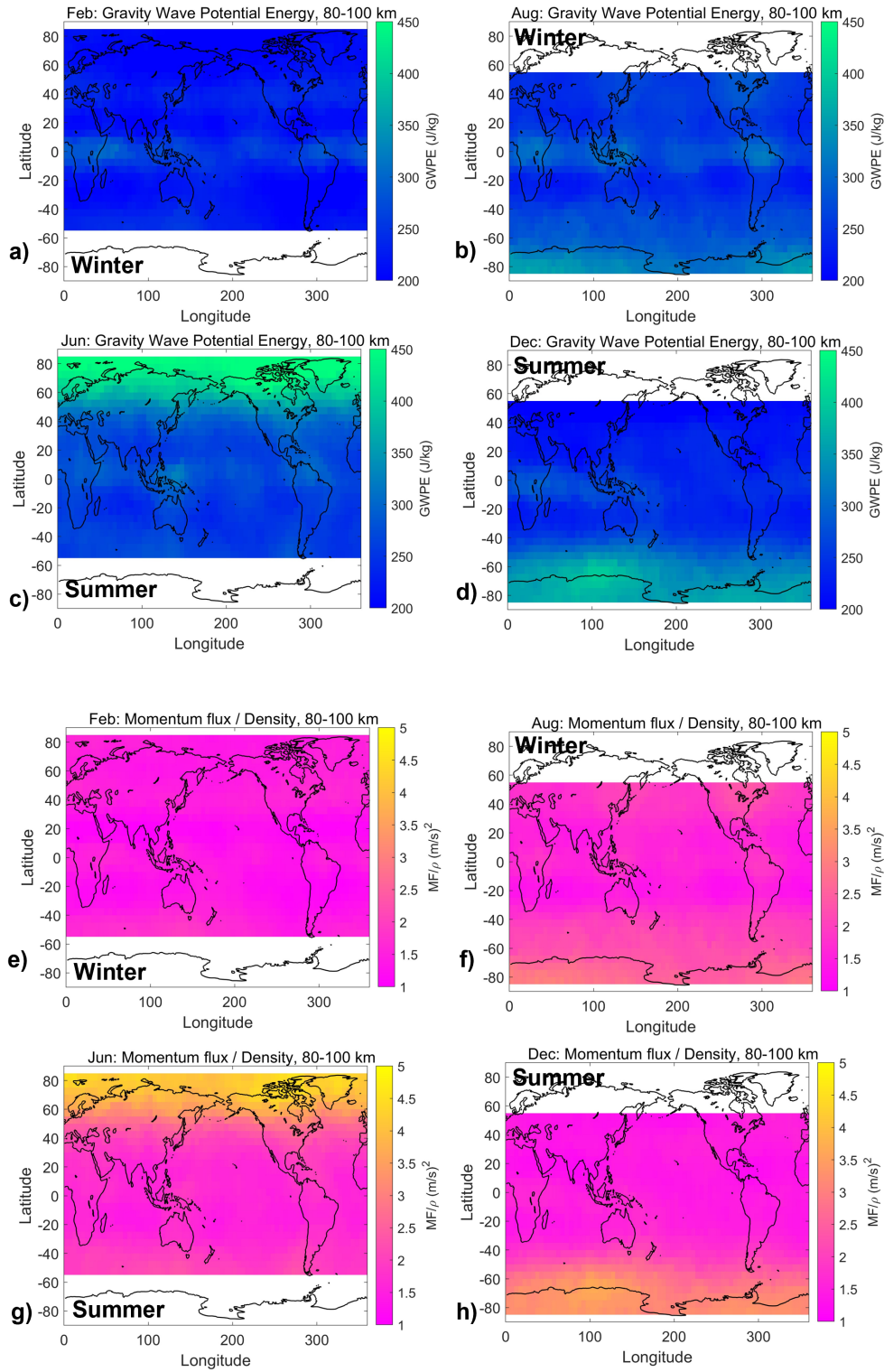


Figure 9. Climatology of GWPE (a-d) and MF/ρ (e-h). The left and right columns show Northern and Southern hemisphere climatologies, respectively. Winter season is given in (a,b,e and f) while summer in (c,d,g and h). Note, clear enhancements in the GW parameters in summer high latitudes and that the seasonal differences are largest in the Northern hemisphere.

484 Note that the upper mesospheric temperature structures in the high latitudes are
 485 broadly similar during the equinoxes and winter (for example, Figures 2(h), 5 and 6).
 486 The mesopause normally occur between 95 and 100 km in non-summer high latitude re-
 487 gion. However, during high latitude summer, it is well known that the mesopause de-
 488 scends to 85 - 90 km as seen in Figure 4(j-l). Therefore, in summer, the whole wave gen-
 489 eration region due to the auroral heating (both Joule and particle heating) lies in a steep
 490 lower thermospheric temperature gradient that could suppress the GWs.

491 Climatologies of GWPE and MF/ρ from SABER measurements between 2002 and
 492 2018 are shown in Figure 9. Panels (a-d) show GWPE and (e-h) show MF/ρ . The left
 493 (right) panels in the Figure show Northern (Southern) Hemispheric winter and summer
 494 seasons as alternating rows. Because of yaw changes of the TIMED satellite, coverage
 495 is poor at latitudes $> 55^\circ$ in one of the hemispheres even in the climatological averages
 496 and hence the variations are separately shown for the Northern and Southern Hemispheres.
 497 Two aspects can be clearly seen from the Figure: (i) wave activity in summer high lat-
 498 itudes are significantly higher in the altitude region of 80 - 100 km in both the hemispheres.
 499 Already existing strong wave activity during summer may reduce the contribution from
 500 geomagnetic activity compared to other seasons, resulting in a weaker summer response.
 501 (ii) the extent of the difference between winter and summer is greater in the Northern
 502 Hemisphere than the Southern Hemisphere (compare Figure 9(a and c) with (b and d)
 503 for GWPE and (e and g) with (f and h) for MF/ρ). Given that hemispheric asymmetries
 504 are an interesting contemporary research topic (Yan et al., 2021; Ern et al., 2022; Hong
 505 et al., 2023), the exact cause of such climatological differences needs further attention.

506 Also, the GW climatology during winter and equinoxes appears similar. We have
 507 not shown the climatologies for the equinoxes herein. Due to the yaw changes of SABER
 508 satellite, the data coverage for the climatologies for Autumn is better than those for spring.
 509 The Autumn climatologies for the month of October in the Northern hemisphere and
 510 for April in the Southern hemisphere closely resemble that of the winter climatologies
 511 in the respective hemispheres (i.e. Figure 9(a) and (e) are similar for climatology of Oc-
 512 tober and (b) and (f) for April). Therefore, the generation mechanisms, propagation con-
 513 ditions and pre-existing GW activity are broadly similar between the winter and equinoxes,
 514 while differing from that of summer both due to the temperature structure and due to
 515 large pre-existing GW activity.

516 Even during non-summer periods, the enhanced GW activity is seen only in 48%
 517 of cases. It is possible that chemical cooling effects due to nitric oxide may play a role
 518 in determining the GW response for a particular event. Improved upper-atmospheric mod-
 519 eling may aid understanding of the processes that lead to enhanced wave activity in some
 520 events and not in others. Moreover, a detailed study on the pattern of particle precip-
 521 itations and their relationship to observed GW enhancements might provide better in-
 522 sights on the interplay between wave generation and background conditions. It is rec-
 523 ognized that each geomagnetic event is different and the effects they produce are also
 524 largely variable. With the available information on temperatures up to 110 km, we are
 525 unable to experimentally establish the underlying cause for enhanced wave forcing in some
 526 events but not on some others, irrespective of seasons.

527 5 Summary and conclusion

528 This work shows for the first time the geographical regions and the altitudes from
 529 where the geomagnetic disturbances become an important GW source. We show that
 530 the geomagnetic activity generated GWs are dominant in the upper mesospheric region
 531 above 80 km in the high latitudes where particle precipitation along the magnetic field
 532 lines occur. The observed GW enhancements coincide with the duration of geomagnetic
 533 activity. No consistent GW enhancements are seen in the lower altitudes or latitudes be-
 534 low 55° . Noteworthy is the seasonality in the GW response to geomagnetic disturbances

535 wherein the summer hemisphere showed weakest response. This appears to be due to
 536 the lower mesopause altitude in summer along with a steep temperature gradient in the
 537 85 - 100 km region and larger pre-existing wave activity. We see a clear reduction in the
 538 mesopause height during non-summer periods owing to the heating by geomagnetic dis-
 539 turbance.

540 Nevertheless, the response in GW activity for geomagnetic disturbances is irreg-
 541 ular in all the seasons in that only 42% of the cases show an unambiguous increase in
 542 the GW activity. During non-summer periods, the percentage increases slightly to 48%.
 543 Therefore, in any particular case, there is no certainty in the enhancement of GW ac-
 544 tivity. This indicates that the pre-existing GWs excited by other lower atmospheric sources
 545 and background wind conditions combine with the forcing from geomagnetic activity in
 546 determining GW variability around a particular event. Detailed cases studies combin-
 547 ing both satellite and ground based measurements will help to gain a better understand-
 548 ing of reason behind some events not showing significant wave enhancements despite in-
 549 tense geomagnetic disturbances like that of 17 March 2015 superstorm.

551 6 Acknowledgements

552 The SABER/TIMED data used in this work can be obtained from [https://saber](https://saber.gats-inc.com/)
 553 [.gats-inc.com/](https://wdc.kugi.kyoto-u.ac.jp/), and AE and Dst indices from <https://wdc.kugi.kyoto-u.ac.jp/>.
 554 This work is supported by NERC project MesoS2D with grant numbers NE/V01837X/1,
 555 NE/V018426/1. CW is supported by Royal Society Fellowship URF\R\221023. NH is
 556 supported by NE/W003201/1 and NE/S00985X/1. PN is supported by a NERC GW4+
 557 Doctoral Training Partnership studentship NE/S007504/1.

558 References

- 559 Alexander, M. J., Gille, J., Cavanaugh, C., Coffey, M., Craig, C., Eden, T., ...
 560 Dean, V. (2008). Global estimates of gravity wave momentum flux from
 561 High Resolution Dynamics Limb Sounder observations. *Journal of Geo-*
 562 *physical Research: Atmospheres*, *113*(D15). Retrieved from [https://](https://agupubs.onlinelibrary.wiley.com/doi/abs/10.1029/2007JD008807)
 563 agupubs.onlinelibrary.wiley.com/doi/abs/10.1029/2007JD008807 doi:
 564 <https://doi.org/10.1029/2007JD008807>
- 565 Alken, P., Thébault, E., Beggan, C. D., Amit, H., Aubert, J., Baerenzung, J., ... et
 566 al. (2021). International geomagnetic reference field: The Thirteenth genera-
 567 tion. *Earth, Planets and Space*, *73*(1). doi: 10.1186/s40623-020-01288-x
- 568 Blanc, E., Ceranna, L., Hauchecorne, A., Charlton-Perez, A., Marchetti, E., Evers,
 569 L. G., ... et al. (2017). Toward an improved representation of middle atmo-
 570 spheric dynamics: thanks to the arise project. *Surveys in Geophysics*, *39*(2),
 571 171–225. doi: 10.1007/s10712-017-9444-0
- 572 Ern, M., Preusse, P., Alexander, M. J., & Warner, C. D. (2004). Absolute val-
 573 ues of gravity wave momentum flux derived from satellite data. *Journal of*
 574 *Geophysical Research: Atmospheres*, *109*(D20). Retrieved from [https://](https://agupubs.onlinelibrary.wiley.com/doi/abs/10.1029/2004JD004752)
 575 agupubs.onlinelibrary.wiley.com/doi/abs/10.1029/2004JD004752 doi:
 576 <https://doi.org/10.1029/2004JD004752>
- 577 Ern, M., Preusse, P., & Riese, M. (2022). Intermittency of gravity wave potential
 578 energies and absolute momentum fluxes derived from infrared limb sounding
 579 satellite observations. *Atmospheric Chemistry and Physics*, *22*(22), 15093–
 580 15133. Retrieved from [https://acp.copernicus.org/articles/22/15093/](https://acp.copernicus.org/articles/22/15093/2022/)
 581 [2022/](https://doi.org/10.5194/acp-22-15093-2022) doi: 10.5194/acp-22-15093-2022
- 582 Esplin, R., Mlynczak, M. G., Russell, J., Gordley, L., & Team, T. S. (2023). Soun-
 583 ding of the Atmosphere using Broadband Emission Radiometry (SABER):

- Instrument and science measurement description. *Earth and Space Science*, 10, e2023EA002999. doi: <https://doi.org/10.1029/2023EA002999>
- Fleming, E. L., Chandra, S., Burrage, M. D., Skinner, W. R., Hays, P. B., Solheim, B. H., & Shepherd, G. G. (1996). Climatological mean wind observations from the UARS high-resolution Doppler imager and wind imaging interferometer: Comparison with current reference models. *Journal of Geophysical Research: Atmospheres*, 101(D6), 10455-10473. Retrieved from <https://agupubs.onlinelibrary.wiley.com/doi/abs/10.1029/95JD01043> doi: <https://doi.org/10.1029/95JD01043>
- Fritts, D. C., & Alexander, M. J. (2003). Gravity wave dynamics and effects in the middle atmosphere. *Reviews of Geophysics*, 41(1). Retrieved from <https://agupubs.onlinelibrary.wiley.com/doi/abs/10.1029/2001RG000106> doi: <https://doi.org/10.1029/2001RG000106>
- García-Comas, M., López-Puertas, M., Marshall, B. T., Wintersteiner, P. P., Funke, B., Bermejo-Pantaleón, D., ... Russell III, J. M. (2008). Errors in Sounding of the Atmosphere using Broadband Emission Radiometry (SABER) kinetic temperature caused by non-local-thermodynamic-equilibrium model parameters. *Journal of Geophysical Research: Atmospheres*, 113(D24). Retrieved from <https://agupubs.onlinelibrary.wiley.com/doi/abs/10.1029/2008JD010105> doi: <https://doi.org/10.1029/2008JD010105>
- Gottelman, A., Mills, M. J., Kinnison, D. E., Garcia, R. R., Smith, A. K., Marsh, D. R., ... Randel, W. J. (2019). The Whole Atmosphere Community Climate Model Version 6 (WACCM6). *Journal of Geophysical Research: Atmospheres*, 124(23), 12380-12403. Retrieved from <https://agupubs.onlinelibrary.wiley.com/doi/abs/10.1029/2019JD030943> doi: <https://doi.org/10.1029/2019JD030943>
- Gordley, L. L., Hervig, M. E., Fish, C., Russell, J. M., Bailey, S., Cook, J., ... Kemp, J. (2009). The solar occultation for ice experiment. *Journal of Atmospheric and Solar-Terrestrial Physics*, 71(3), 300-315. Retrieved from <https://www.sciencedirect.com/science/article/pii/S136468260800206X> (Global Perspectives on the Aeronomy of the Summer Mesopause Region) doi: <https://doi.org/10.1016/j.jastp.2008.07.012>
- Harding, B. J., Makela, J. J., Englert, C. R., Marr, K. D., Harlander, J. M., England, S. L., & Immel, T. J. (2017). The MIGHTI wind retrieval algorithm: Description and verification. *Space Science Reviews*, 212(1-2), 585-600. doi: [10.1007/s11214-017-0359-3](https://doi.org/10.1007/s11214-017-0359-3)
- Harvey, V. L., Pedatella, N., Becker, E., & Randall, C. (2022). Evaluation of Polar Winter Mesopause Wind in WACCMX+DART. *Journal of Geophysical Research: Atmospheres*, 127(15), e2022JD037063. Retrieved from <https://agupubs.onlinelibrary.wiley.com/doi/abs/10.1029/2022JD037063> doi: <https://doi.org/10.1029/2022JD037063>
- Hertzog, A., Alexander, M. J., & Plougonven, R. (2012). On the intermittency of gravity wave momentum flux in the stratosphere. *Journal of the Atmospheric Sciences*, 69(11), 3433 - 3448. Retrieved from <https://journals.ametsoc.org/view/journals/atmsc/69/11/jas-d-12-09.1.xml> doi: <https://doi.org/10.1175/JAS-D-12-09.1>
- Hindley, N. P., Mitchell, N. J., Cobbett, N., Smith, A. K., Fritts, D. C., Janches, D., ... Moffat-Griffin, T. (2022). Radar observations of winds, waves and tides in the mesosphere and lower thermosphere over South Georgia island (54 S, 36 W) and comparison with WACCM simulations. *Atmospheric Chemistry and Physics*, 22(14), 9435-9459. Retrieved from <https://acp.copernicus.org/articles/22/9435/2022/> doi: [10.5194/acp-22-9435-2022](https://doi.org/10.5194/acp-22-9435-2022)
- Hindley, N. P., Wright, C. J., Smith, N. D., Hoffmann, L., Holt, L. A., Alexander, M. J., ... Mitchell, N. J. (2019). Gravity waves in the winter stratosphere over the southern ocean: high-resolution satellite observations and 3-d spectral

- 639 analysis. *Atmospheric Chemistry and Physics*, 19(24), 15377–15414. Re-
 640 trieved from <https://acp.copernicus.org/articles/19/15377/2019/> doi:
 641 10.5194/acp-19-15377-2019
- 642 Hong, Y., Deng, Y., Zhu, Q., Maute, A., Hairston, M. R., Waters, C., ... Lopez,
 643 R. E. (2023). Inter-hemispheric asymmetries in high-latitude electrodynamic
 644 forcing and the thermosphere during the October 8-9, 2012, geomagnetic
 645 storm: An integrated data -model investigation. *Frontiers in Astronomy
 646 and Space Sciences*, 10. Retrieved from [https://www.frontiersin.org/
 647 articles/10.3389/fspas.2023.1062265](https://www.frontiersin.org/articles/10.3389/fspas.2023.1062265) doi: 10.3389/fspas.2023.1062265
- 648 Hunsucker, R. D. (1982). Atmospheric gravity waves generated in the high-latitude
 649 ionosphere: A review. *Reviews of Geophysics*, 20(2), 293-315. Retrieved
 650 from [https://agupubs.onlinelibrary.wiley.com/doi/abs/10.1029/
 651 RG020i002p00293](https://agupubs.onlinelibrary.wiley.com/doi/abs/10.1029/RG020i002p00293) doi: <https://doi.org/10.1029/RG020i002p00293>
- 652 Jin, H., Miyoshi, Y., Fujiwara, H., Shinagawa, H., Terada, K., Terada, N., ... Saito,
 653 A. (2011). Vertical connection from the tropospheric activities to the iono-
 654 spheric longitudinal structure simulated by a new Earth's whole atmosphere-
 655 ionosphere coupled model. *Journal of Geophysical Research: Space Physics*,
 656 116(A1). Retrieved from [https://agupubs.onlinelibrary.wiley.com/doi/
 657 abs/10.1029/2010JA015925](https://agupubs.onlinelibrary.wiley.com/doi/abs/10.1029/2010JA015925) doi: <https://doi.org/10.1029/2010JA015925>
- 658 John, S. R., & Kumar, K. K. (2012). TIMED/SABER observations of global grav-
 659 ity wave climatology and their interannual variability from stratosphere to
 660 mesosphere lower thermosphere. *Climate Dynamics*, 39(6), 1489-1505. doi:
 661 10.1007/s00382-012-1329-9
- 662 McDonald, A. J. (2012). Gravity wave occurrence statistics derived from paired
 663 COSMIC/FORMOSAT3 observations. *Journal of Geophysical Research: At-
 664 mospheres*, 117(D15). Retrieved from [https://agupubs.onlinelibrary
 665 .wiley.com/doi/abs/10.1029/2011JD016715](https://agupubs.onlinelibrary.wiley.com/doi/abs/10.1029/2011JD016715) doi: [https://doi.org/10.1029/
 666 2011JD016715](https://doi.org/10.1029/2011JD016715)
- 667 McLandress, C., Shepherd, G. G., Solheim, B. H., Burrage, M. D., Hays, P. B.,
 668 & Skinner, W. R. (1996). Combined mesosphere/thermosphere winds us-
 669 ing WINDII and HRDI data from the Upper Atmosphere Research Satel-
 670 lite. *Journal of Geophysical Research: Atmospheres*, 101(D6), 10441-10453.
 671 Retrieved from [https://agupubs.onlinelibrary.wiley.com/doi/abs/
 672 10.1029/95JD01706](https://agupubs.onlinelibrary.wiley.com/doi/abs/10.1029/95JD01706) doi: <https://doi.org/10.1029/95JD01706>
- 673 Mertens, C. J., Russell III, J. M., Mlynczak, M. G., She, C.-Y., Schmidlin, F. J.,
 674 Goldberg, R. A., ... Xu, X. (2009). Kinetic temperature and carbon diox-
 675 ide from broadband infrared limb emission measurements taken from the
 676 TIMED/SABER instrument. *Advances in Space Research*, 43(1), 15-27.
 677 Retrieved from [https://www.sciencedirect.com/science/article/pii/
 678 S0273117708002883](https://www.sciencedirect.com/science/article/pii/S0273117708002883) doi: <https://doi.org/10.1016/j.asr.2008.04.017>
- 679 Narayanan, V. L., Gurubaran, S., & Emperumal, K. (2012). Nightglow imag-
 680 ing of different types of events, including a mesospheric bore observed on
 681 the night of February 15, 2007 from Tirunelveli (8.7 N). *Journal of Atmo-
 682 spheric and Solar-Terrestrial Physics*, 78-79, 70-83. Retrieved from [https://
 683 www.sciencedirect.com/science/article/pii/S136468261100215X](https://www.sciencedirect.com/science/article/pii/S136468261100215X) doi:
 684 <https://doi.org/10.1016/j.jastp.2011.07.006>
- 685 Noble, P., Hindley, N., Wright, C., Cullens, C., England, S., Pedatella, N., ...
 686 Moffat-Griffin, T. (2022). Interannual variability of winds in the antarctic
 687 mesosphere and lower thermosphere over rothera (67°S, 68°W) in radar
 688 observations and waccm-x. *Atmospheric Chemistry and Physics Discussions*,
 689 2022, 1–29. Retrieved from [https://acp.copernicus.org/preprints/
 690 acp-2022-150/](https://acp.copernicus.org/preprints/acp-2022-150/) doi: 10.5194/acp-2022-150
- 691 Oyama, S., & Watkins, B. J. (2012). Generation of Atmospheric Gravity Waves
 692 in the Polar Thermosphere in Response to Auroral Activity. *Space Science Re-
 693 views*, 168, 463-473. doi: 10.1007/s11214-011-9847-z

- 694 Ramkumar, T., Gurubaran, S., & Rajaram, R. (2002). Lower E-region MF radar
695 spaced antenna measurements over magnetic equator. *Journal of Atmospheric*
696 *and Solar-Terrestrial Physics*, *64*(12), 1445-1453. Retrieved from [https://](https://www.sciencedirect.com/science/article/pii/S1364682602001086)
697 www.sciencedirect.com/science/article/pii/S1364682602001086 doi:
698 [https://doi.org/10.1016/S1364-6826\(02\)00108-6](https://doi.org/10.1016/S1364-6826(02)00108-6)
- 699 Reid, I. M. (2015). MF and HF radar techniques for investigating the dynamics and
700 structure of the 50 to 110 km height region: a review. *Progress in Earth and*
701 *Planetary Science*, *2*, 33. doi: 10.1186/s40645-015-0060-7
- 702 Remsberg, E. E., Marshall, B. T., Garcia-Comas, M., Krueger, D., Lingenfelter,
703 G. S., Martin-Torres, J., ... Thompson, R. E. (2008). Assessment of the qual-
704 ity of the Version 1.07 temperature-versus-pressure profiles of the middle atmo-
705 sphere from TIMED/SABER. *Journal of Geophysical Research: Atmospheres*,
706 *113*(D17). Retrieved from [https://agupubs.onlinelibrary.wiley.com/doi/](https://agupubs.onlinelibrary.wiley.com/doi/abs/10.1029/2008JD010013)
707 [abs/10.1029/2008JD010013](https://agupubs.onlinelibrary.wiley.com/doi/abs/10.1029/2008JD010013) doi: <https://doi.org/10.1029/2008JD010013>
- 708 Roble, R. G., & Ridley, E. C. (1994). A thermosphere-ionosphere-mesosphere-
709 electrodynamics general circulation model (Time-GCM): Equinox solar cycle
710 minimum simulations (30–500 km). *Geophysical Research Letters*, *21*(6), 417-
711 420. Retrieved from [https://agupubs.onlinelibrary.wiley.com/doi/abs/](https://agupubs.onlinelibrary.wiley.com/doi/abs/10.1029/93GL03391)
712 [10.1029/93GL03391](https://agupubs.onlinelibrary.wiley.com/doi/abs/10.1029/93GL03391) doi: <https://doi.org/10.1029/93GL03391>
- 713 Shepherd, G. G., Thuillier, G., Cho, Y.-M., Duboin, M.-L., Evans, W. F. J.,
714 Gault, W. A., ... Ward, W. E. (2012). The Wind Imaging Interferom-
715 eter (WINDII) on the Upper Atmosphere Research Satellite: A 20 year
716 perspective. *Reviews of Geophysics*, *50*(2). Retrieved from [https://](https://agupubs.onlinelibrary.wiley.com/doi/abs/10.1029/2012RG000390)
717 agupubs.onlinelibrary.wiley.com/doi/abs/10.1029/2012RG000390 doi:
718 <https://doi.org/10.1029/2012RG000390>
- 719 Siskind, D. E., Jones Jr., M., Drob, D. P., McCormack, J. P., Hervig, M. E., Marsh,
720 D. R., ... Mitchell, N. J. (2019). On the relative roles of dynamics and
721 chemistry governing the abundance and diurnal variation of low-latitude
722 thermospheric nitric oxide. *Annales Geophysicae*, *37*(1), 37–48. Retrieved
723 from <https://angeo.copernicus.org/articles/37/37/2019/> doi:
724 [10.5194/angeo-37-37-2019](https://doi.org/10.5194/angeo-37-37-2019)
- 725 Smith, A. K. (2012). Global Dynamics of the MLT. *Surveys in Geophysics*, *33*(6),
726 1177–1230. doi: 10.1007/s10712-012-9196-9
- 727 Smith, A. K., Pedatella, N. M., Marsh, D. R., & Matsuo, T. (2017). On the Dy-
728 namical Control of the Mesosphere - Lower Thermosphere by the Lower and
729 Middle Atmosphere. *Journal of the Atmospheric Sciences*, *74*(3), 933 - 947.
730 Retrieved from [https://journals.ametsoc.org/view/journals/atsc/74/3/](https://journals.ametsoc.org/view/journals/atsc/74/3/jas-d-16-0226.1.xml)
731 [jas-d-16-0226.1.xml](https://journals.ametsoc.org/view/journals/atsc/74/3/jas-d-16-0226.1.xml) doi: <https://doi.org/10.1175/JAS-D-16-0226.1>
- 732 Stober, G., Kuchar, A., Pokhotelov, D., Liu, H., Liu, H.-L., Schmidt, H., ...
733 Mitchell, N. (2021). Interhemispheric differences of mesosphere-lower ther-
734 mosphere winds and tides investigated from three whole-atmosphere models
735 and meteor radar observations. *Atmospheric Chemistry and Physics*, *21*(18),
736 13855–13902. Retrieved from [https://acp.copernicus.org/articles/21/](https://acp.copernicus.org/articles/21/13855/2021/)
737 [13855/2021/](https://acp.copernicus.org/articles/21/13855/2021/) doi: 10.5194/acp-21-13855-2021
- 738 Stockwell, R., Mansinha, L., & Lowe, R. (1996). Localization of the complex spec-
739 trum: the S transform. *IEEE Transactions on Signal Processing*, *44*(4), 998-
740 1001. doi: 10.1109/78.492555
- 741 Wright, C. J., & Gille, J. C. (2013). Detecting overlapping gravity waves using the
742 S-Transform. *Geophysical Research Letters*, *40*(9), 1850-1855. Retrieved from
743 <https://agupubs.onlinelibrary.wiley.com/doi/abs/10.1002/grl.50378>
744 doi: <https://doi.org/10.1002/grl.50378>
- 745 Wright, C. J., Hindley, N. P., Moss, A. C., & Mitchell, N. J. (2016). Multi-
746 instrument gravity-wave measurements over Tierra del Fuego and the Drake
747 Passage - Part 1: Potential energies and vertical wavelengths from AIRS,
748 COSMIC, HIRDLS, MLS-Aura, SAAMER, SABER and radiosondes. *Atmo-*

- 749 *spheric Measurement Techniques*, 9(3), 877–908. Retrieved from [https://](https://amt.copernicus.org/articles/9/877/2016/)
750 amt.copernicus.org/articles/9/877/2016/ doi: 10.5194/amt-9-877-2016
- 751 Wright, C. J., Rivas, M. B., & Gille, J. C. (2011). Intercomparisons of HIRDLS,
752 COSMIC and SABER for the detection of stratospheric gravity waves. *At-*
753 *mospheric Measurement Techniques*, 4(8), 1581–1591. Retrieved from
754 <https://amt.copernicus.org/articles/4/1581/2011/> doi: 10.5194/
755 amt-4-1581-2011
- 756 Wu, C., & Ridley, A. J. (2023). Comparison of TIDI line of sight winds with ICON-
757 MIGHTI measurements. *Journal of Geophysical Research: Space Physics*,
758 128(2), e2022JA030910. Retrieved from [https://agupubs.onlinelibrary](https://agupubs.onlinelibrary.wiley.com/doi/abs/10.1029/2022JA030910)
759 [.wiley.com/doi/abs/10.1029/2022JA030910](https://agupubs.onlinelibrary.wiley.com/doi/abs/10.1029/2022JA030910) doi: [https://doi.org/10.1029/](https://doi.org/10.1029/2022JA030910)
760 2022JA030910
- 761 Yan, X., Konopka, P., Hauck, M., Podglajen, A., & Ploeger, F. (2021). Asymmetry
762 and pathways of inter-hemispheric transport in the upper troposphere and
763 lower stratosphere. *Atmospheric Chemistry and Physics*, 21(9), 6627–6645.
764 Retrieved from <https://acp.copernicus.org/articles/21/6627/2021/>
765 doi: 10.5194/acp-21-6627-2021
- 766 Zawdie, K., Belehaki, A., Burleigh, M., Chou, M.-Y., Dhadly, M. S., Greer, K., ...
767 Zhang, S.-R. (2022). Impacts of acoustic and gravity waves on the iono-
768 sphere. *Frontiers in Astronomy and Space Sciences*, 9. Retrieved from
769 <https://www.frontiersin.org/articles/10.3389/fspas.2022.1064152>
770 doi: 10.3389/fspas.2022.1064152

1 **Observations of mesospheric gravity waves generated**
2 **by geomagnetic activity**

3 **V. L. Narayanan**¹, **C. Wright**¹, **M. Mlynczak**², **N. Hindley**¹, **A. Kavanagh**³,
4 **T. Moffat-Griffin**³, **P. Noble**^{1,3}

5 ¹Center for Climate Adaptation and Environment Research, Department of Electronic and Electrical
6 Engineering, University of Bath, Bath, UK
7 ²NASA Langley Research Center, Hampton, USA
8 ³British Antarctic Survey, Cambridge, UK

9 **Key Points:**

- 10 • Geomagnetically forced gravity waves penetrate down to ~80 km only in the high
11 latitude regions as revealed by SABER temperature data
12 • Summer high latitude mesosphere is less responsive for gravity wave generation
13 due to geomagnetic activity
14 • Mesopause descends in the high latitudes except for summer season during intense
15 geomagnetic disturbances

Corresponding author: V. L. Narayanan, narayananvlwins@gmail.com, lnv23@bath.ac.uk

Abstract

Gravity waves (GWs) play an important role in the dynamics and energetics of the mesosphere. Geomagnetic activity is a known source of GWs in the upper atmosphere. However, how deep the effects of geomagnetic activity induced GWs penetrate into the mesosphere remains an open question. We use temperature measurements from the SABER/TIMED instrument between 2002 - 2018 to study the variations of mesospheric GW activity following intense geomagnetic disturbances identified by AE and Dst indices. By considering several case studies, we show for the first time that the GWs forced by geomagnetic activity can propagate down to about 80 km in the high latitude mesosphere. Only regions above 55° latitudes show a clear response. The fraction of cases in which there is an unambiguous enhancement in GW activity following the onset of geomagnetic disturbance is smaller during summer than other seasons. Only about half of the events show an unambiguous increase in GW activity during non-summer periods and about one quarter of the events in summer show an enhancement in GWs. In addition, we also find that the high latitude mesopause is seen to descend in altitude following onset of geomagnetic activity in the non-summer high latitude region.

Plain Language Summary

Gravity waves (GWs) exist throughout the atmosphere and are crucial in the dynamics of the middle and upper atmosphere. A variety of processes are known to excite GWs at different altitudes. Above 100 km, space weather induced geomagnetic activity is an important source for the GWs. However, how deep such waves penetrate into the mesosphere, and in what latitude regions their effect is important remains unknown. In this work, we use SABER/TIMED satellite measurements of temperature between 2002 - 2018 to investigate this question. For the first time, we find that the geomagnetic activity forces mesospheric GWs only in the high latitude regions, where enhanced energy deposition occurs along magnetic field lines. Further, these GWs occur only above 80 km, and no unambiguous signature is seen at lower heights. Though damping is expected due to the increasing atmospheric density, this work identifies the altitude and latitude extent for such GWs forced by geomagnetic activity in the mesosphere. Further, there is a significant seasonality in the response such that summer hemisphere shows weakest GW generation due to geomagnetic activity. The mesopause height is also observed to descend during intense geomagnetic disturbances occurring in non-summer periods.

1 Introduction

Atmospheric gravity waves (GWs) are oscillations in the atmosphere spanning a wide range of spatio-temporal scales. Their horizontal sizes range from few 100 m to few 1000 km, with vertical scales of few 100 m to few 10s of km, and time periods vary from about 5 min to several hours, upper limit determined depending on the latitude of observations (Fritts & Alexander, 2003). These waves are forced by different processes in different regions of the atmosphere and propagate away from the source region carrying energy and momentum. They play a crucial role in the vertical coupling of the atmosphere-ionosphere system. The importance of GWs in the upper mesosphere is now well recognized, and the counter-intuitive latitudinal temperature structure of the mesosphere is understood to result from GW driven circulation (Smith, 2012; Blanc et al., 2017). One of the earliest identified sources of upper atmospheric GWs was geomagnetic disturbances (Hunsucker, 1982; Oyama & Watkins, 2012) and it is well known that thermospheric GWs affect the ionosphere and manifest as traveling ionospheric disturbances, though the finer details of this plasma-neutral coupling process remains an active area of research (Zawdie et al., 2022). While the importance of geomagnetic activity as a GW source is well recognized for the thermosphere and E- and F-region ionosphere, the extent to which its dominance penetrates into the middle atmosphere is not properly investigated. It is ex-

66 pected that wave amplitudes will be damped when they propagate downwards due to
67 the exponentially increasing atmospheric density, but it remains unknown how deep ge-
68 omagnetic activity induced GWs occur. Furthermore, prior to this study we do not know
69 if this effect in the middle atmosphere is global or restricted only to the high latitudes.
70 Neither we know about any seasonality in the mesospheric GW response to geomagnetic
71 activity.

72 These aspects remain unknown due to the lack of sufficient data above 70 km at
73 the required spatio-temporal scales. With increasing computational power, modelling of
74 the atmosphere has improved significantly, but most such models focus on the troposphere
75 and stratosphere. Several models are capable of providing physical parameters and chem-
76 ical constituents of the mesosphere, yet GWs are not resolved and tend to be parame-
77 terized. For example the Whole Atmosphere Community Climate Model (WACCM) (Gettelman
78 et al., 2019; Smith et al., 2017), and the Ground-to-topside Atmosphere Ionosphere model
79 for Aeronomy (GAIA) (Jin et al., 2011). Both can include aspects of ionospheric elec-
80 trodynamics to varying degrees. The Thermosphere - Ionosphere - Mesosphere Electro-
81 dynamics - Global Circulation Model (TIME-GCM) is a widely used model in upper at-
82 mosphere - ionosphere studies. It differs from the above mentioned models in that the
83 lower boundary of the model is at stratospheric heights (Roble & Ridley, 1994). Yet, TIME-
84 GCM also uses GW parameterization and suffers from the lack of required spatio tem-
85 poral resolutions to study GW generation from geomagnetic activity. Further, none of
86 these models capture finer variations in the temperature and wind in the mesosphere at
87 the required resolution (Siskind et al., 2019; Harvey et al., 2022; Hindley et al., 2022; Sto-
88 ber et al., 2021; Noble et al., 2022).

89 Ground based measurements are available up to about 100 km but they are typ-
90 ically restricted by geographical location which make it impossible to understand the ef-
91 fects in the global context. An important drawback for ground based radio remote sens-
92 ing of mesospheric neutral wind measurements is that the measured winds are signifi-
93 cantly affected by the ionospheric variability occurring above 90 km (Ramkumar et al.,
94 2002; Reid, 2015). Geomagnetic activity often results in increased contamination from
95 the ionospheric processes at heights above 90 km. Airglow measurements can also pro-
96 vide information about the upper mesosphere, specifically imaging technique is capable
97 of observing different types of waves and instability structures (e.g., Narayanan et al.,
98 2012). However, in the high latitudes, auroral contamination makes imaging of GWs nearly
99 impossible during geomagnetically active times hindering a study of mesospheric GW
100 response using airglow imagers. Therefore, it is important to combine different type of
101 ground based measurements to properly address this problem, for example, combining
102 radar, airglow and lidar measurements. Co-existence of such diverse measurements from
103 single location is extremely rare. Gathering different types of ground based mesospheric
104 measurements from multiple sites to study the mesospheric GW variability correspond-
105 ing to geomagnetic activity has not been accomplished yet.

106 Space based remote sensing from artificial satellites provide an opportunity to mea-
107 sure the atmosphere globally. Many limb sounding and nadir viewing swath measure-
108 ments of atmospheric parameters like temperature and radiance have been used in the
109 past to study GWs (Ern et al., 2004; Alexander et al., 2008; Wright et al., 2011; John
110 & Kumar, 2012; Wright et al., 2016). However, most satellite measurements provide in-
111 formation on neutral atmosphere only to ~ 70 km altitude from the surface. Space based
112 ionospheric measurements are often made in the F-region heights. As a result, the re-
113 gion from 70 - 120 km is unfortunately not well measured with satellite remote sensing.

114 There are some noticeable exceptions to this limited coverage of the 70-120km range
115 like the Wind Imaging Interferometer (WINDII) (Shepherd et al., 2012) and the High
116 Resolution Doppler Imager (HRDI) payloads (McLandress et al., 1996; Fleming et al.,
117 1996) onboard the Upper Atmosphere Research Satellite (UARS) satellite. UARS flew
118 in the early 1990s, but the satellite inclination was low enough that high latitude wind

119 measurements were not available. Further, the measurements had a day-night difference
 120 in the altitude coverage as well. Sounding of the Atmosphere using Broadband Emis-
 121 sion Radiometry (SABER) and TIMED Doppler Interferometer (TIDI) are the payloads
 122 designed to measure temperature and winds, respectively, and flown onboard Thermo-
 123 sphere - Ionosphere - Mesosphere Energetics and Dynamics (TIMED) satellite (Remsberg
 124 et al., 2008; Mertens et al., 2009; Wu & Ridley, 2023). SABER measures temperature
 125 and some minor constituents. TIDI measures four separate line of sight winds and it ap-
 126 pears to have problems in getting proper vector wind estimates continuously (Wu & Ri-
 127 dley, 2023). The Solar Occultation For Ice Experiment (SOFIE) onboard Aeronomy of
 128 Ice in the Mesosphere (AIM) satellite measures temperatures but only during sunrise and
 129 sunset hours of each orbit leaving only ~ 30 profiles at different locations in a day (Gordley
 130 et al., 2009). Recently, the Ionospheric CONnection explorer (ICON) mission had the
 131 Michelson Interferometer for Global High-resolution Thermospheric Imaging (MIGHTI)
 132 payload capable of measuring neutral winds but the satellite is of a low inclination or-
 133 bit not covering middle and higher latitude regions (Harding et al., 2017). Among these,
 134 SABER temperatures have been measured continuously from January 2002 with an al-
 135 titude coverage from upper troposphere to 110 km and near-global spatial coverage. There-
 136 fore, SABER is suitable for studying the importance of space weather sources in gen-
 137 erating GWs into the middle atmosphere. The temperatures are retrieved both during
 138 day and night with reliable error estimates upto about 110 km (Remsberg et al., 2008;
 139 García-Comas et al., 2008). Hence we use SABER data for this study and the analysis
 140 method is explained in the next section.

141 This is the first study to investigate mesospheric GWs forced by geomagnetic ac-
 142 tivity in a global context. This is an important component of space weather impacts on
 143 the middle atmosphere. Further, the observational results provided here are expected
 144 to help formulate model improvements for the upper mesospheric region.

145 2 Data Analysis

146 2.1 Event identification

147 Since our aim is to understand the role of geomagnetic activity in the forcing of
 148 mesospheric GWs, we ensure only the strongest events are selected in order to study the
 149 effects unambiguously. We use AE and Dst indices to identify the events. AE index is
 150 widely used to study the auroral activity and substorm occurrences. AE index is derived
 151 from a set of magnetometers in the northern hemispheric auroral region. The Dst index
 152 is derived from a set of low-mid latitude magnetometer stations and mainly indicates the
 153 ring current and its enhancements. Dst index is used to identify the geomagnetic storms.
 154 First, we focused on major geomagnetic storms having minimum Dst ≤ -200 nT and those
 155 extreme events with a high threshold of AE ≥ 1500 nT. This identified 24 events between
 156 2002 and 2018. Once the AE index reaches beyond 1500 nT, we find the time when the
 157 AE index start to rise above 300 nT. We define this time as start of the event. Short pe-
 158 riod fluctuations of AE < 300 nT are allowed if occurring for less than 8 continuous hours,
 159 so that rapid fluctuations before a major event are accounted for.

160 To improve statistics and check that the results from detailed event-based analy-
 161 sis hold for relatively weaker geomagnetic disturbances, we also identified all events with
 162 maximum AE ≥ 1000 nT. The start for such events is taken as the AE index reaching
 163 300 nT and remaining quasi-continuously high. By quasi-continuous, we allow fluctu-
 164 ations below 300 nT but not for ≥ 8 hours. Often the AE indices will fluctuate above 1000
 165 nT a few times during such intense geomagnetic activity periods. We merge such fluc-
 166 tuations into a single event. In this way, 248 events were identified to perform a seasonal
 167 and hemispherical statistics between 2002 and 2018.

168

2.2 SABER/TIMED data analysis

169

170

171

172

173

174

175

176

177

178

179

180

We use temperature measurements from the SABER instrument onboard the TIMED satellite obtained between 2002 and 2018. The instrument measures limb radiances between 1.27 and 16.9 μm in 10 channels from which temperature and other minor species concentrations are retrieved. Detailed description of the instrument and retrievals can be found elsewhere (Esplin et al., 2023). The latitudinal coverage alternates between 83°N – 52°S and 52°N – 83°S every 60 - 63 days, resulting in coverage of high latitudes only in one of the hemispheres at any given time. The SABER scan is designed such that adjacent profiles are separated alternatively by ~ 250 km and ~ 450 km distances along the track at the upper mesospheric tangent heights. The instantaneous field of view of the instrument is ~ 2 km but the retrievals are made at a finer spacing of about 0.4-0.5 km altitude steps. We apply a 2 km smoothing and resample the data at 1 km vertical intervals. Three such successive profiles are shown in Figure 1(a-c).

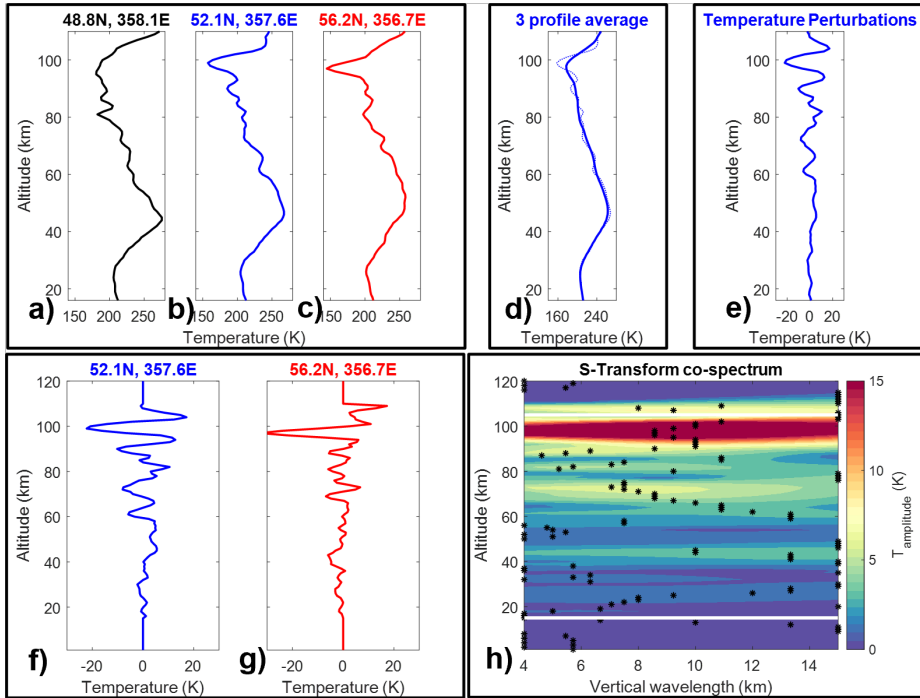


Figure 1. a-c) Three adjacent temperature profiles at 1 km vertical spacing after applying 2 km smoothing (see text for details), d) Thick line shows the 7 km Average of the three profiles shown in panel 'b' which is taken as the background for the center profile (also shown with dotted lines), e) Temperature perturbations obtained after subtracting the background, f-g) Zero padded temperature perturbation profiles, h) Amplitude co-spectra of S-Transform of the profiles. The stars shows the maximum amplitude wave at each altitude which is considered for further calculations of GWPE and MF.

181

182

183

184

185

186

187

In SABER data, each data point in a profile is associated with a latitude, longitude, solar local time (SLT) and universal time (UT). We average these values for each profile between 15 - 110 km heights to represent a mean location and time for the profile. To obtain a background for a particular temperature profile, the adjacent profiles along the satellite track are taken together and a 7 km vertical running average is made on the three profile combination. This background profile is shown in Figure 1(d). The thin dotted line shows the original profile. By subtracting the estimated background pro-

188 file from each profile, we obtain temperature perturbations that are predominantly con-
 189 tributed by GWs (Figure 1(e)). For background estimation, 7 km was selected for the
 190 running average in the vertical after considering a range of step sizes. For smaller step
 191 sizes, many GWs will be included in the background and when it is larger, the mesopause
 192 and any sharp inversion layers will be smoothed out in the background temperature un-
 193 realistically. The latter will generate large perturbation temperatures that are not real
 194 when subtracting the estimated background temperature profile. At the same time, we
 195 note that 7 km coincides with mean scale height. When making background tempera-
 196 ture estimations in this way, the intrinsic assumption is that the background is smooth
 197 over about 700 km in the horizontal, i.e. the average distance covered between 3 pro-
 198 files in the along-track direction.

199 An S-transform analysis is applied to temperature perturbation profiles (Figure 1(e))
 200 following past works (e.g., Stockwell et al., 1996; Alexander et al., 2008; Wright et al.,
 201 2016; Hindley et al., 2019). Hindley et al. (2019) discusses in detail the S-transform cal-
 202 culation that has been adopted herein. The complex output of S-transform of each pro-
 203 file is multiplied by the complex conjugate of the adjacent profile's S-transform to ob-
 204 tain a complex co-spectrum. Figure 1(f-g) shows the adjacent temperature perturbation
 205 profiles zero padded to reduce edge effects resulting in the amplitude co-spectrum shown
 206 in Figure 1(h). The maximum values of the co-spectrum at each altitude is assumed to
 207 represent the dominant wave at that particular altitude. From the magnitude of the com-
 208 plex co-spectrum peak, we obtain the square of the wave amplitude in temperature. By
 209 dividing the phase with the distance between adjacent profiles, we obtain the horizon-
 210 tal wavenumber of the dominant wave (see Alexander et al. (2008); Wright and Gille (2013)
 211 for more details). The corresponding frequency of the co-spectral peak gives the verti-
 212 cal wavenumber. In this way, we obtain an estimate of the amplitude of the dominant
 213 wave perturbation, its vertical and horizontal wavenumbers. Note that we restrict the
 214 vertical scales of the S-transform to 4 - 15 km. The upper limit is aimed at suppressing
 215 long vertical wavelength tidal contributions while the lower limit ensures both the Nyquist
 216 criterion is met and the altitude extent of any instability/turbulence region in the at-
 217 mosphere does not affect the wave results. Because we study geomagnetic disturbances
 218 spanning a few days, the longitudinal coverage is sparse and hence we use zonal aver-
 219 age of the GW parameters in our study.

220 **2.3 Gravity wave potential energy and Momentum flux calculations**

221 From the estimated wave parameters, gravity wave potential energy (GWPE) and
 222 pseudo-momentum fluxes (MF) are obtained from the following relations. Pseudo-momentum
 223 flux will simply be referred as momentum flux hereafter.

$$E_P = \frac{1}{2} \frac{g^2}{N^2} \left(\frac{T'}{\bar{T}} \right)^2 \quad (1)$$

$$M_f = \frac{\rho \lambda_v}{2 \lambda_h} \frac{g^2}{N^2} \left(\frac{T'}{\bar{T}} \right)^2 = E_P \rho \frac{\lambda_z}{\lambda_h} \quad (2)$$

224 Where, E_P and M_f represents GWPE and MF (the vertical flux of horizontal momen-
 225 tum) respectively (Ern et al., 2004). g and ρ stand for acceleration due to gravity and
 226 density respectively. We used the densities provided by SABER data and account for
 227 the variation of g with height. λ_h and λ_v represent the horizontal and vertical wavelengths
 228 obtained from cospectral analysis. T' is the perturbation temperature and \bar{T} is the back-
 229 ground temperature. We can calculate GWPE using (i) the temperature perturbations
 230 obtained as the amplitude of spectral analysis which correspond to the dominant wave
 231 mode at a height and pair of profiles (the temperature value indicated by the stars in
 232 Figure 1(e) as done in Alexander et al. (2008), for example), and (ii) also using the raw

233 temperature perturbations obtained after subtracting the background temperature es-
 234 timates assuming the contributions from turbulence and tides are negligible compared
 235 to GWs. While the latter assumption is a rudimentary one, the variabilities appear to
 236 be similar in both the potential energy estimates and we prefer to use the ones calcu-
 237 lated from the spectral analysis. The term N in the equation is the buoyancy frequency
 238 calculated from the measured temperature and its gradient as below,

$$N^2 = \frac{g}{T} \left(\frac{dT}{dz} + \frac{g}{C_P} \right) \quad (3)$$

239 where g/C_P is the dry adiabatic lapse rate with C_P , the specific heat at constant pres-
 240 sure taken as $1005 \text{ JKg}^{-1}\text{K}^{-1}$. This is justified because the topmost region considered
 241 in our study is still around the turbopause and the atmosphere remains well mixed. We
 242 divide the momentum flux by atmospheric density (MF/ρ) to result in units of m^2/s^2 ,
 243 which is dimensionally similar to the wind variances due to GWs. This aids in better
 244 visualization of variation with altitude because MF usually given in units of Pa , which
 245 decrease exponentially with height.

246 In the above discussion, the GWs identified are affected by the instrument obser-
 247 vational filter effect, i.e. the sensitivity of a measurement technique to a range of GW
 248 frequencies and wavelengths. No instrument is capable of measuring the whole spectrum
 249 of GWs. The observational filter of SABER is estimated in Figure 9 of Wright et al. (2016).
 250 Because the cospectrum is computed in the satellite's along-track direction, any wavevec-
 251 tor oriented orthogonal to the track will not be observed. For a wave propagating in an
 252 arbitrary direction, the wave vector's projection along the satellite track is identified and
 253 hence the measured horizontal wavenumber is less than the real wavenumber in the hor-
 254 izontal indicating that the measured momentum flux will be less as well. Hence, we are
 255 measuring only a part of the momentum flux from a portion of the GW spectrum that
 256 is restricted by observational filter effect of the instrument. Therefore, we will not fo-
 257 cus on the absolute quantification and the magnitude of the GW momentum fluxes. Rather
 258 we will focus on the relative changes and variations before, during and after the geomag-
 259 netic activity in this work. This realization also enables us to adopt a computationally
 260 efficient way to study the wave variabilities by selecting the dominant wave signature from
 261 the S-Transform instead of selecting waves above a particular threshold or significance
 262 level. This approach is widely used (Alexander et al., 2008; Wright & Gille, 2013; Wright
 263 et al., 2016; Hertzog et al., 2012; McDonald, 2012).

264 To check if there is an unambiguous enhancement following geomagnetic activity,
 265 we calculate GWPE and MF/ρ for 48 hours before and after the start of the event. This
 266 is not based on UT days but is a zonal average of the data for 48 hours before and af-
 267 ter the hour of onset. Note that as described in section 2.1, the start is when the AE reaches
 268 and quasi-continuously stays above 300 nT. The percentage change (C) is evaluated as,

$$C = \frac{(P_{aft} - P_{bef})}{P_{bef}} .100 \quad (4)$$

269 where, P_{bef} and P_{aft} are the 48 hour averages of GWPE or MF/ρ before and after the
 270 onset, respectively. When the mean C between 85 and 100 km altitudes is above +10%
 271 for either GWPE or MF/ρ , it is considered to indicate an unambiguous generation of
 272 GW due to the geomagnetic activity. This threshold of +10% is determined as follows.
 273 Three sets of 500 random dates and times are selected and the 48 hour averages of GWPE
 274 and MF/ρ are calculated and subjected to equation 4. Percentiles of variation are cal-
 275 culated and in all three sets, 10% threshold lies above 85th percentile of the calculated
 276 variations for both GWPE and MF/ρ . It may be noted that the random samplings may
 277 also contain periods of higher geomagnetic activity. No geomagnetic indices are consid-
 278 ered when randomly sampling the start dates. Effectively, 48 hours before and after 500
 279 random samples sum upto 2000 equivalent days resulting in about 5.5 years of randomly

Table 1. Seasons and number of events identified

Seasons	Northern Hemisphere			Southern Hemisphere		
	Duration	No. of. Events		Duration	No. of. Events	
		AE \geq 1500 nT	AE \geq 1000 nT		AE \geq 1500 nT	AE \geq 1000 nT
Winter	22 Oct - 21 Feb	4	34	22 Apr - 21 Aug	7	57
Vernal	22 Feb - 21 Apr	1	14	22 Aug - 21 Oct	2	19
Summer	22 Apr - 21 Aug	4	43	22 Oct - 21 Feb	3	19
Autumn	22 Aug - 21 Oct	1	28	22 Feb - 21 Apr	2	34

280 selected data in each of the sample set. The threshold fixed from such an approach should
 281 be a meaningful one.

282 2.4 Seasonal separation

283 We consider a month on either side of the equinox days as equinoctial periods: Febru-
 284 ary 22 - April 21 and August 22 - October 21. Periods outside these ranges are consid-
 285 ered to represent either summer or winter solstice based on the high latitude hemisphere
 286 covered by the satellite. Table 1 shows the periods considered as summer, winter and
 287 equinoxes in this study along with the number of events identified for different AE thresh-
 288 olds.

289 3 Results

290 3.1 Case Studies

291 3.1.1 Winter observations

292 Figure 2(a) and (b) shows the Dst and AE indices around one of the strongest ge-
 293 omagnetic event of this century, which started on 29 October 2003. The event was a ge-
 294 omagnetic superstorm with a double dip in the Dst index plummeting below -350 nT
 295 and with an AE index crossing 2000 nT. Figure 2(c-f) shows the daily zonal mean of GW
 296 parameters from 90 to 100 km altitude separated into 5 degree latitude bins. GWPE,
 297 Temperature perturbations and MF/ρ (panels (c-e)) show a clear enhancement in wave
 298 activity poleward of $55^\circ N$ during geomagnetic disturbance (see Doy 302 - 306). Verti-
 299 cal wavelengths (Figure 2(f)) show an enhancement during the geomagnetic event around
 300 the same latitude regions where an enhanced wave activity is noticed. Note that these
 301 vertical wavelengths are also zonal averages in 5 degree latitudinal bins. This indicates
 302 that relatively longer vertical wavelength GWs are observed following the storm.

303 Figure 2(g) shows the altitude profiles of GWPE and MF/ρ obtained 48 hours be-
 304 fore (dashed lines) and 48 hours following the storm onset (continuous lines). The re-
 305 gion spanning magnetic inclination of $60^\circ - 90^\circ$ in the Northern hemisphere are aver-
 306 aged herein to obtain the figure since the satellite coverage is in that hemisphere. Av-
 307 eraging with respect to the magnetic inclination values instead of geographic latitude band
 308 is necessary since energy deposition during geomagnetic disturbances directly occur in
 309 the regions with higher magnetic inclinations (and therefore higher magnetic latitudes).
 310 The magnetic inclination values at 100 km altitude are obtained from IGRF 13 model
 311 (Alken et al., 2021). Figure 2(g) shows an unambiguous enhancement of the wave ac-
 312 tivity from about 80 km following the geomagnetic storm. For the first time, this clearly
 313 shows the depth to which dynamic effects of geomagnetic activity penetrates directly.

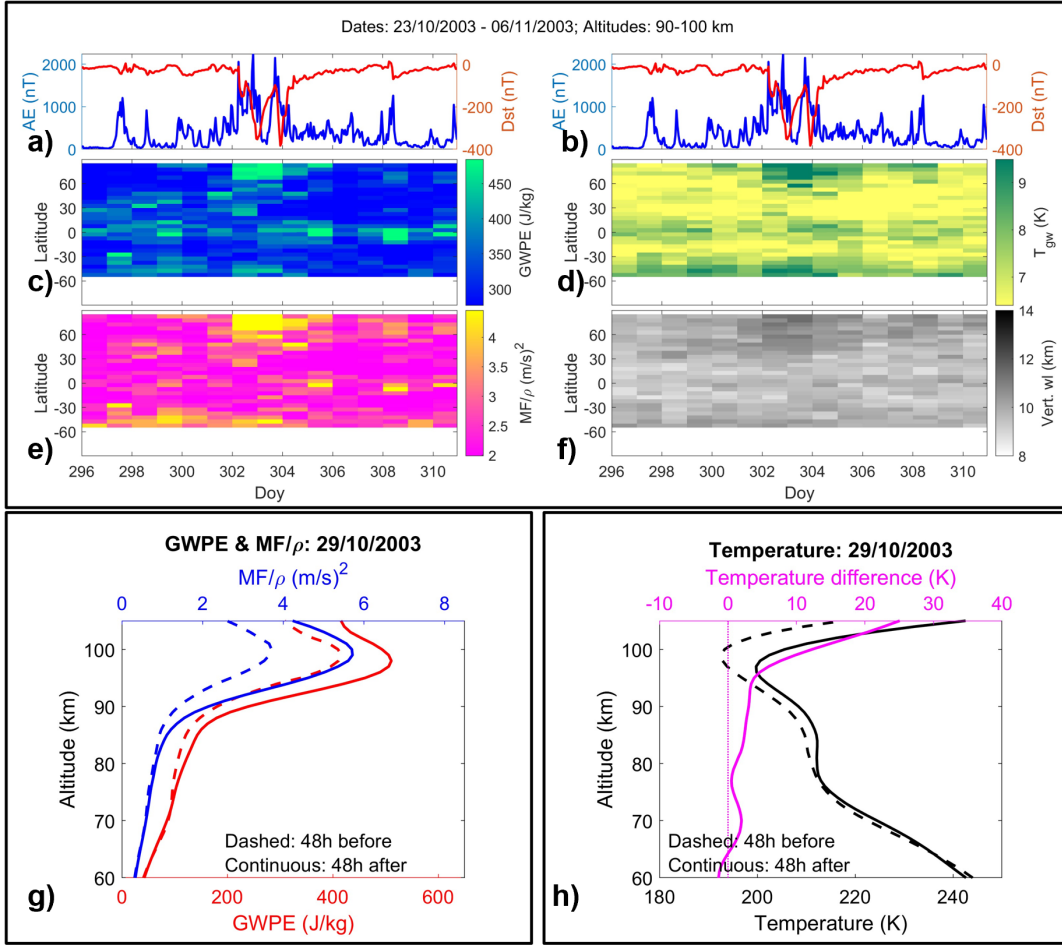


Figure 2. Geomagnetic superstorm of 29 October 2003. a and b) AE and Dst indices, c) GWPE, d) Temperature perturbations before subjecting to spectral analysis, e) MF/ρ , f) Vertical wavelengths. All the parameters in panels c - f are daily longitudinal averages at 5 degree latitude bins. g) Altitude profiles of average GWPE and MF/ρ from 60 – 90° magnetic inclinations in the Northern hemisphere for 48 hours before and after onset of geomagnetic event, and h) Zonal average temperature profiles from 60 – 90° magnetic inclinations for 48 hours before and after the onset of geomagnetic event in black, and the temperature difference in magenta (after - before).

314 Figure 2(h) shows the 48 hour average of temperature profiles before and after the
 315 storm onset plotted in black, calculated for the same geographic region as in Figure 2(g).
 316 This shows the effect of intense geomagnetic activity on the upper mesospheric temper-
 317 ature. There is a heating due to the enhanced geomagnetic activity as can be seen from
 318 the higher temperature values post storm onset. This is better visualized with the mag-
 319 neta curve showing the difference between temperatures after and before the storm onset,
 320 i.e. difference between the continuous and dashed black curves. In addition, the alti-
 321 tude of the mesopause descends as a result of the heating as revealed by the black lines
 322 in Figure 2(h). This is typical for all the events identified except in the summer hemi-
 323 sphere, as will be shown later.

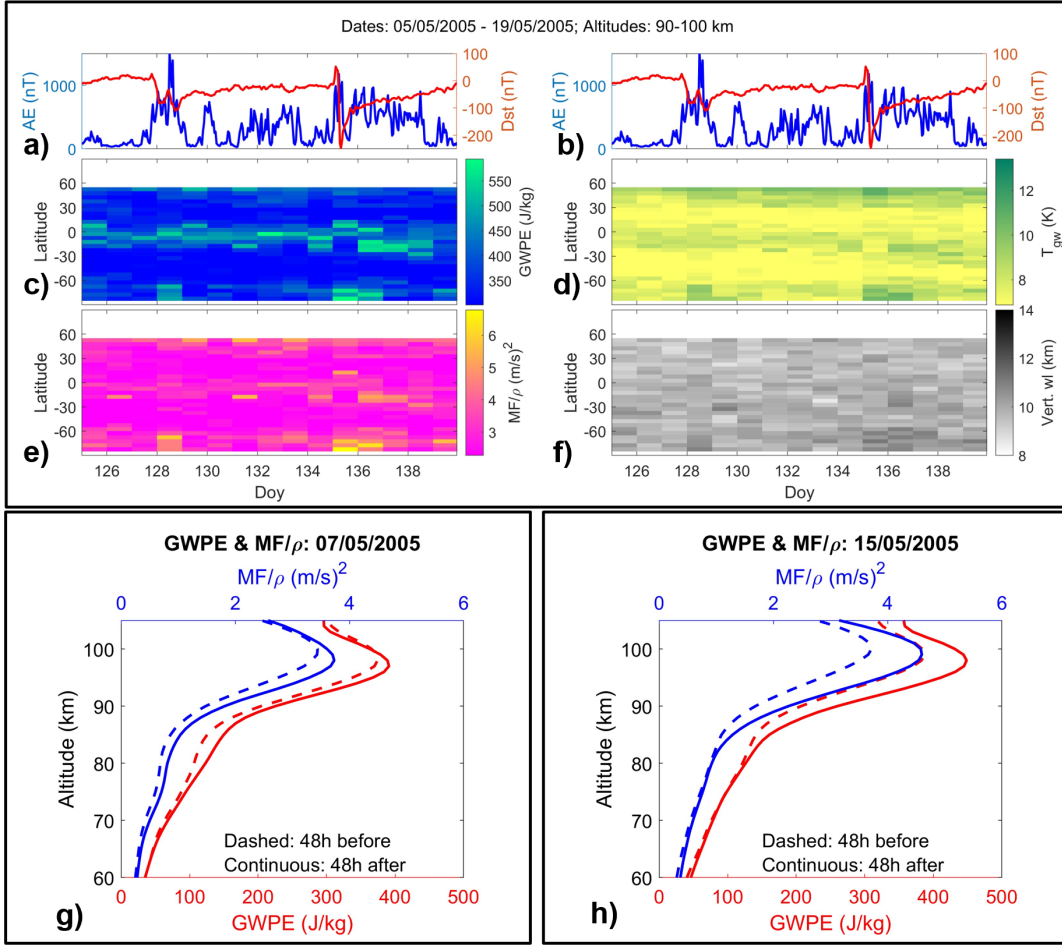


Figure 3. Events of 7 and 15 May 2005. a and b) AE and Dst indices, c) GWPE, d) Temperature perturbations without subjecting to spectral analysis, e) MF/ρ , f) Vertical wavelengths. g and h) Altitude profiles of average GWPE and MF/ρ from $60 - 90^\circ$ magnetic inclinations in the Southern hemisphere for 48 hours before and after the onset respectively for 7 and 15 May 2005.

324 Figure 3 show the results for two events during May 2005. During this period SABER
 325 was covering Southern high latitudes and hence these were observed in winter. The first
 326 event is a compound substorm which started on 7 May and continued until 8 May 2005.
 327 There was only a moderate geomagnetic storm during this period as can be inferred from
 328 the Dst index reaching a minimum close to -100 nT. The second event is that of the major
 329 geomagnetic storm of 15 May 2005 (day of the year (Doy) 135) when the Dst indices
 330 reached below -200 nT (Figure 3(a) and (b)). Though the peak value of AE is higher
 331 during 7-8 May 2005, the event of 15 May 2005 continued for about 3 days and resulted
 332 in one of the severe geomagnetic storms and hence is the stronger prolonged event amongst
 333 the two. From the GWPE, MF/ρ and temperature perturbations (Figure 3(c, e and d)),
 334 it is clear that there is an enhanced wave activity on 8 May 2005 (Doy 128) and 15 and
 335 16 May 2005 (Doy 135 and 136). Similar to the case of 29 October 2003, the vertical wave-
 336 lengths show a coincident enhancement (Figure 3(f)) during both the events in the high
 337 latitudes. Another noticeable feature in Figure 3(c-f) is that the period of 9 - 14 May
 338 2005 is not quiet. Though the AE index has not reached extremely high values of 1000
 339 nT, the period has had significant geomagnetic substorm events and auroral activity. There
 340 are intermittent weaker enhancements in GW activity as well, for example, on days 132

and 133. These observations confirm that intense substorms like that of 7-8 May 2005 also generate GWs into the mesosphere. This implies that the physical processes behind the GW generation are similar for major geomagnetic storms and strong substorms.

Figure 3(g) and (h) respectively show the altitude profiles of average GWPE and MF/ρ for the compound substorm of 7 May 2005 and major geomagnetic storm of 15 May 2005. These profiles are averages between magnetic inclination of -60° – -90° in the Southern Hemisphere. The enhancement in GW activity is larger for the stronger event of 15 May 2005. Similar to the event of 29 October 2003 (Figure 2) and that of 7 November 2004 (not shown), a clear increase in GW activity is seen above 80 km for both these events observed during winter. It appears that the direct penetration of GWs ceases around 80 km and hence geomagnetic activity is an important source only in the upper mesosphere. In addition, the neutral temperature behaviour for these two events (not shown) is similar to that of the 29 October 2003 case (Figure 2(h)) in that the mesopause descended along with higher temperature values post storm onset. Similar descent of mesopause was also noticed during severe storm of 7 November 2004 observed by SABER above the northern high latitudes (not shown).

3.1.2 Summer observations

Figure 4 shows three events in June - July 2005 with onset dates of 12 June (Doy 163), 22 June (Doy 173) and 09 July (Doy 190), respectively. All three events had large AE indices indicating very strong substorm activity, but were only moderate geomagnetic storms with Dst around -100 nT (Figure 4(a) and (b)). Note that generally there is enhanced GW activity at high latitudes during summer irrespective of geomagnetic activity associated enhancements (Figure 4(c-f), above $60^\circ N$). Figure 4(g-i) shows the altitude profiles of the average GWPE and MF/ρ between 60° – 90° inclination angles for the three events. For the first event of 12 June 2005, there is a clear enhancement in the wave activity above ~ 88 km (Figure 4(g)). For the second event beginning on 22 June 2005, there is an enhancement in wave activity only above 94 km (Figure 4(h)). This event does not show a +10% change between 85 - 100 km according to our threshold. Evidently, the magnetic activity levels for 22 June event was weaker compared to that of 12 June 2005 (Figure 4(a-b)).

The third case of 9 July 2005 does not show any enhancement in GW activity (Figures 4(i) and 4(c-e)). However, there is a weak enhancement in average vertical wavelengths for the 9 July 2005 case (Figure 4(f)). It appears as if the geomagnetic activity contributed to some wave generation indicated by vertical wavelength enhancement similar to other cases. Nevertheless, the pre-existing wave activity and its variability during summer masks the contribution from geomagnetic activity. Such a scenario could explain the lack of enhanced wave activity in the averaged wave properties like GWPE and MF/ρ while there is an enhancement in the averaged vertical wavelength. Alternatively, it is likely that the power of pre-existing GW variation was already large during this summer event so that the contribution from geomagnetic activity falls below background levels except in the vertical wavenumber. Figure 4(a-f) has been terminated on 14 July 2005 (Doy 195) right at the end of the multi-night compound substorm event of 9 July 2005 due to a change in SABER latitude coverage.

These events are observed in summer high latitudes where the mesopause occurs below 90 km (Figure 4(j-l)). Note that the mesopause height during summer is not affected following onset of geomagnetic activity contrary to other seasons (black curves). Nevertheless, the extent of heating during summer is comparable to other seasons as seen from the temperature difference profiles after and before the geomagnetic disturbances (magenta curves). Interestingly, the heating during 12 June and 9 July 2005 is comparable in strength but the former shows an enhanced GW forcing below 100 km while the

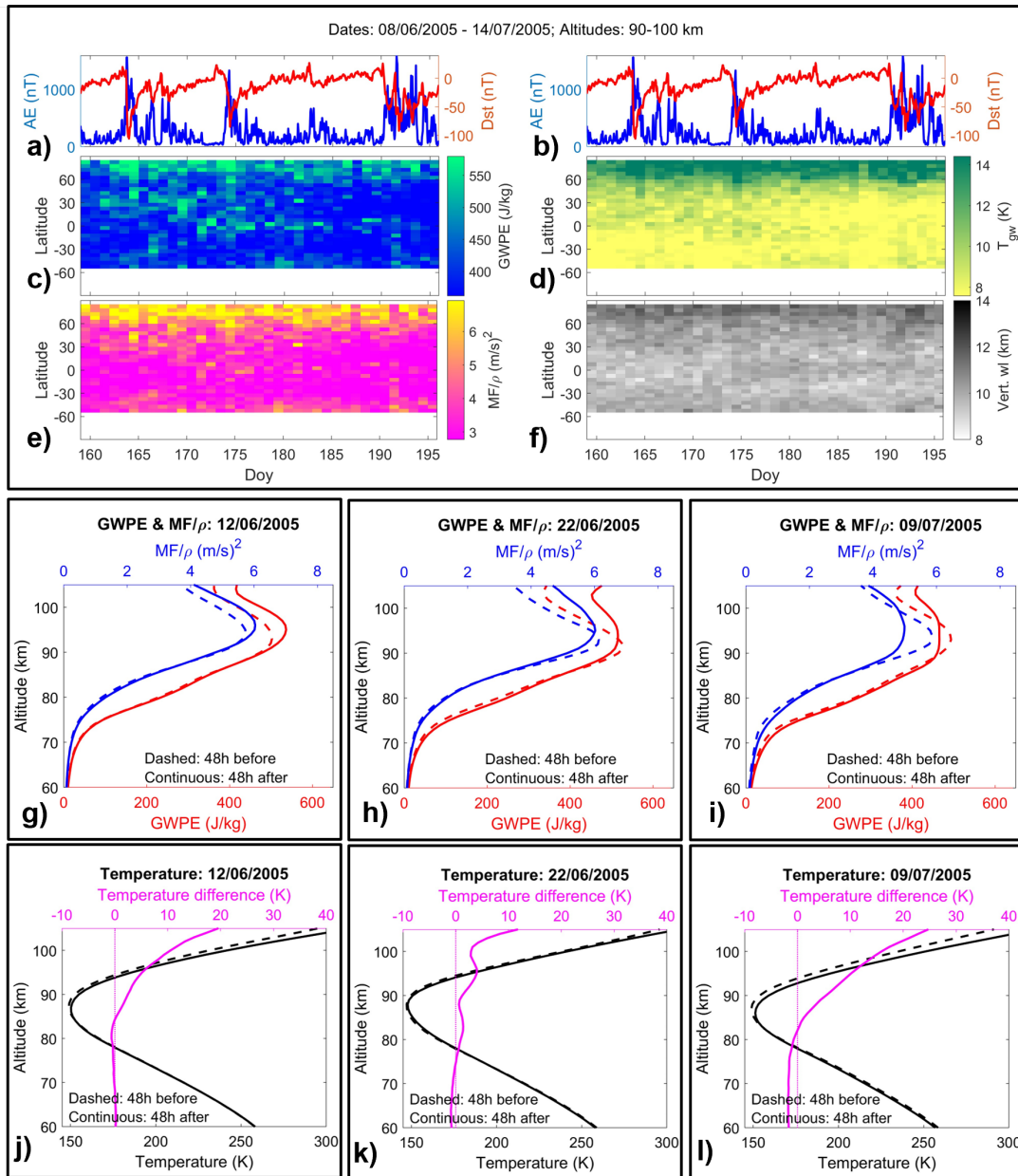


Figure 4. Events of 12 June, 22 June and 9 July 2005. and b) AE and Dst indices, c) GWPE, d) Temperature perturbations without subjecting to spectral analysis, e) MF/ρ , f) Vertical wavelengths.2. g-i) Altitude profiles of zonal average GWPE and MF/ρ 48 hours before and after the geomagnetic disturbances. j-l) Zonal average temperature profiles from 60 – 90° magnetic inclinations for 48 hours before and after the onset of geomagnetic event in black, and the temperature difference post and pre onset in magenta.

391 latter does not. Thus, the summer high latitudes appear to respond in a different man-
 392 ner to the geomagnetic activity as seen above within a span of 30 days.

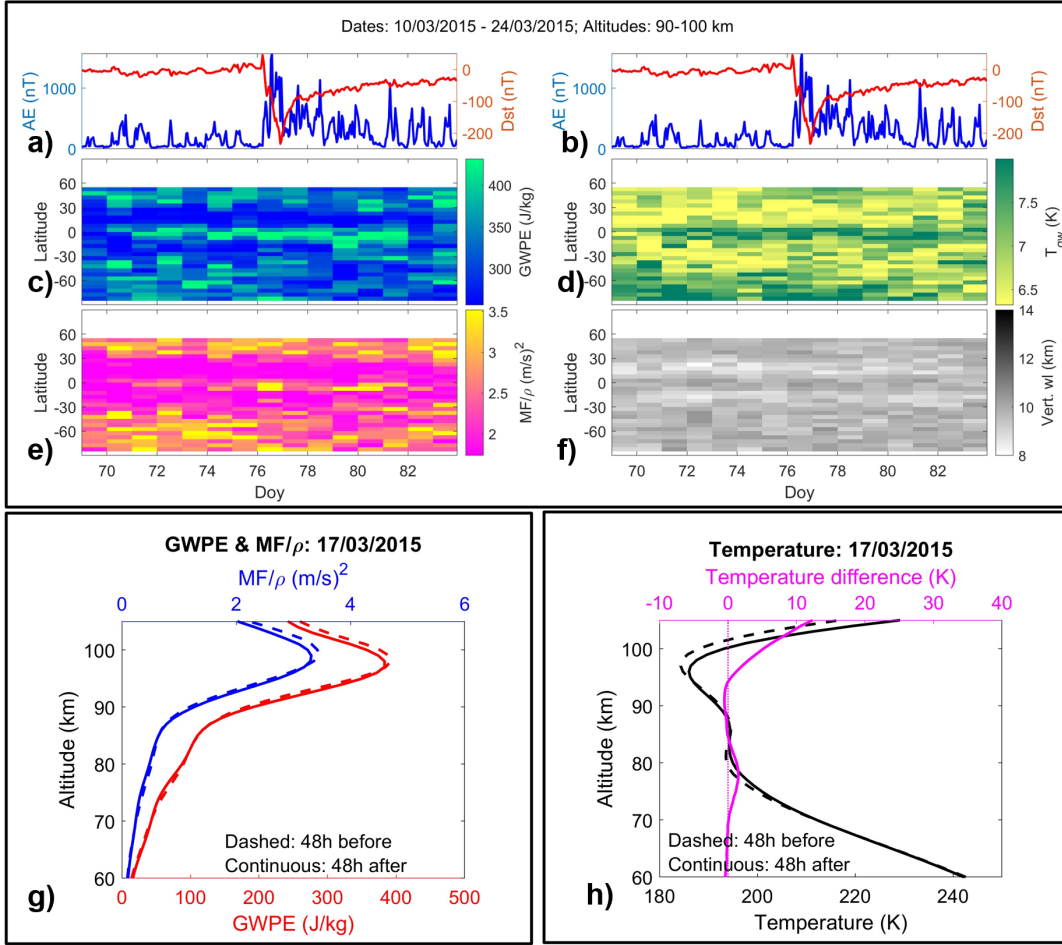


Figure 5. St. Patrick's Day storm of 17 March 2015. Figures are in the same format as that of Figure 2.

393

3.1.3 Equinoctial observations

394

395

396

397

398

399

400

401

402

403

404

405

406

407

408

Figure 5 shows observations during the St. Patrick's Day storm of 17 March 2015. SABER was measuring Southern high latitudes and thus this event falls under Autumn equinox. This was the strongest geomagnetic storm of solar cycle 24. During this event, the Dst index reached -223 nT and the AE index reached 1570 nT with significantly high values (i.e. above 1000 nT) from 17 to 19 March 2015. However, this event did not lead to a noticeable increase in GW activity as seen from Figure 5(c-f). Figure 5(g) showing altitude profiles of GWPE and MF/ρ before and after the event further confirms lack of enhancement in the GW activity. This is surprising when noticing that even compound substorms have been shown to lead to enhanced GW activity (for example, Figures 3 and 4). At the same time, Figure 5(h) displaying that the average temperature profiles before and after the onset of the event still shows a reduction in the mesopause altitude and heating above 90 km. Nevertheless, no enhancement in GW activity is seen. It is worth noting that there was lack of response to another relatively weaker geomagnetic event on 17 March 2013, which was also observed by SABER over the southern high latitudes (not shown).

409

410

On the other hand, another autumn equinox observation during 26 September 2011 shows a noticeable enhancement in GW activity over Northern high latitudes as shown

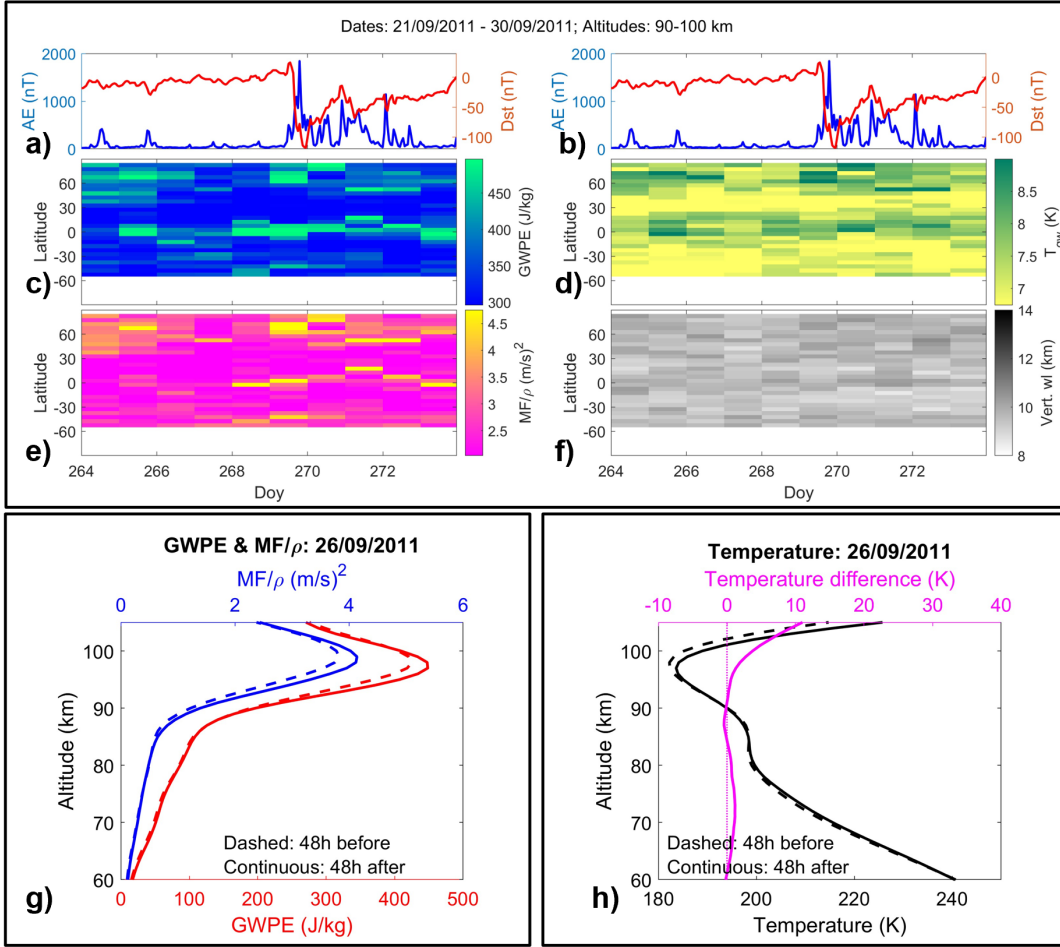


Figure 6. Autumn equinox observation showing an enhancement in GW activity. Figures are in the same format as that of Figure 2.

411 in Figure 6. This event was a compound substorm which co-occurred with a geomag-
 412 netic storm with Dst index of about -100 nT. The St. Patrick's Day storms of 2015 (Fig-
 413 ure 5) and 2013 are more intense geomagnetic events that did not lead to an increase
 414 in GW activity. The 48 hour average temperature profile comparisons before and after
 415 the onset for the event of 26 September 2011 shown in Figure 6(h) indicates similar heat-
 416 ing and a reduction in the mesopause altitude compared to 17 March 2015 event (Fig-
 417 ure 5(h)). This further implies that the GW response does not merely depend on the strength
 418 of heating or the extent of the descent of mesopause. Therefore, other factors like tem-
 419 perature gradient, wind variations and pre-existing wave activity play a role in the ext-
 420 ent of enhancement in the GW activity post onset of a geomagnetic event.

421 Three events occurred during vernal equinox season with $AE \geq 1500$ nT, and two
 422 of them showed a clear enhancement in GW activity following the start of geomagnetic
 423 disturbance. Each hemisphere witnessed one such event (not shown).

424 3.2 Statistics

425 First, we discuss the cases where the maximum AE index is above 1500 nT or min-
 426 imum Dst index below -200 nT from which the individual cases shown in the previous

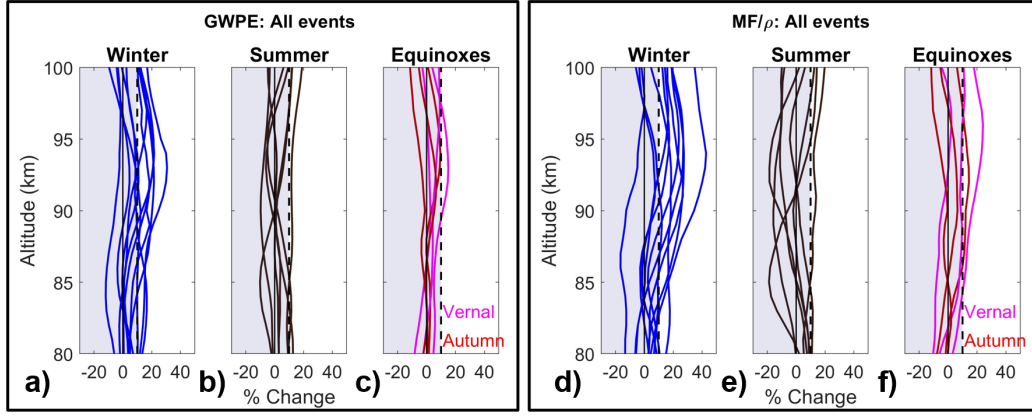


Figure 7. Percentage changes of GWPE for (a) winter, (b) summer and (c) equinoxes, and MF/ρ for (d) winter, (e) summer and (f) equinoxes for the events having threshold values of $AE \geq 1500$ nT or $Dst \leq -200$ nT. The region below +10% is shaded.

427 section are selected. Figure 7(a-c) and (d-f) shows the altitude profiles of percentage changes
 428 of GWPE and MF/ρ , respectively, for all the events selected according to equation 4.
 429 The thin black vertical line indicates 0 and thick dashed black line corresponds to +10%,
 430 our threshold to unambiguously identify a change post onset of geomagnetic activity. The
 431 region below +10% are shaded in Figure 7. Note that most of the winter cases in Figure
 432 7(a) and (d) show positive excursion beyond 10% threshold in the 80 - 100 km alti-
 433 tude range, while only 1 case in summer show a such a behaviour (Figure 7(b) and (e)).
 434 During equinoxes, 3 out of 6 events showed a positive excursion beyond 10% line for MF/ρ
 435 (Figure 7(f)).

436 In order to increase the number of cases and ensure that the statistics discussed
 437 above hold, we proceed to analyze all events with peak $AE > 1000$ nT. Out of the 253
 438 identified events, 5 occurred around the dates of SABER/TIMED yaw change and hence
 439 cannot be used, leaving 248 events for statistical analysis. For these events we calculate
 440 the percentage changes in GWPE and MF/ρ and define an average percentage change
 441 greater than 10% between 85 and 100 km altitudes as a meaningful change. The results
 442 are shown in Figure 8(a) for both the hemispheres and 8(b) and (c) respectively for the
 443 Northern and Southern hemispheres. Figure 8 shows a clear dip in summer in the re-
 444 sponse, in concurrence with our case studies (Figure 7). The responses are similar be-
 445 tween the hemispheres. Statistically, the GW enhancements during equinoxes appear to
 446 be slightly stronger than those during the winter solstice in the Northern hemisphere than
 447 the Southern hemisphere.

488 4 Discussion

449 In this section, we will consolidate the above observations and discuss the reasons
 450 for the observed seasonality in the GW response to geomagnetic activity. As seen from
 451 examples given in Figure 3, 4 and 6, we note that intense substorm activity plays an im-
 452 portant role in affecting the GW variability. It is known that geomagnetic disturbances
 453 may arise from different drivers such as coronal mass ejections, corotating interaction
 454 regions and high-intensity long-duration continuous AE activity (HILDCAA). We did
 455 not separate the events based on the drivers because all of them produce substorms and
 456 almost all intense geomagnetic storms co-occur with strong substorm events. The en-
 457 hancement in GW activity is always observed only in the high latitude regions, and more
 458 importantly they occur in a transient manner nicely coinciding with the periods of ge-

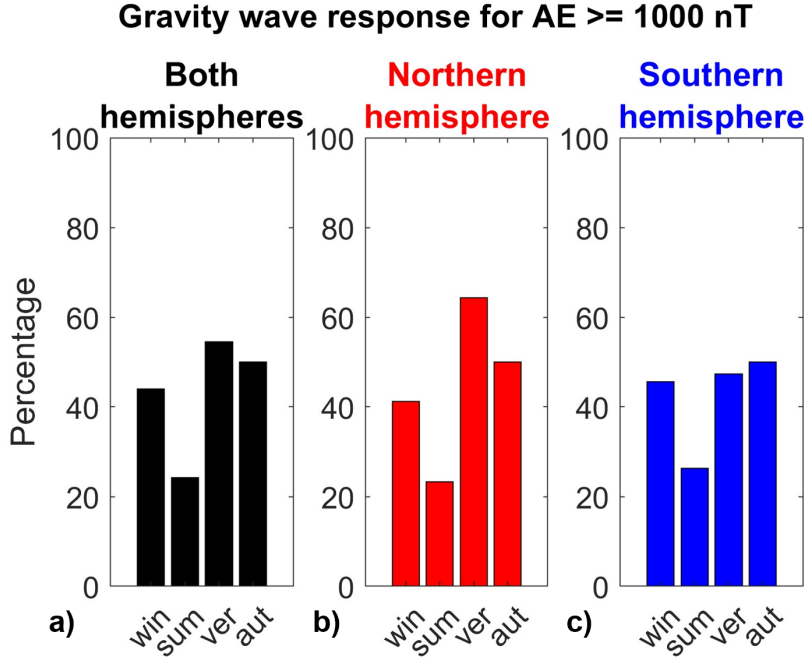


Figure 8. Seasonal and hemispherical response for geomagnetically active events having maximum $AE \geq 1000$ nT .

459 omagnetic disturbances as seen from AE index enhancements (Figures 2 - 6). This in-
 460 dicates that active forcing generates the GWs, i.e. they are not propagating from else-
 461 where. Hence substorm related heating effects appear to be the source for these GWs.

462 Two major GW sources in the high latitude upper atmosphere associated with ge-
 463 omagnetic activity are Joule and particle heating (Oyama & Watkins, 2012). Joule heat-
 464 ing peaks in the region of 120 - 130 km while particle heating peaks at lower altitudes
 465 where the atmospheric density is large enough for frequent collisions. An increase in ver-
 466 tical wavelength coincident with the increased GW activity following geomagnetic dis-
 467 turbances is observed in $\sim 70\%$ of the cases with peak $AE \geq 1500$ nT. This preferen-
 468 tial formation of longer vertical wavelength GWs following geomagnetic activity might
 469 be an indication of the underlying generation mechanism. From the temperature pro-
 470 files shown in Figures 2, 4, 5 and 6, it is seen that heating occurs above 90 km. This im-
 471 plies that particle heating is likely to be the important source responsible for the GWs
 472 observed below 100 km, because heating may occur almost in-situ and immediately above
 473 the region of wave observation. Particle heating may also have a matching vertical scale
 474 length to that of observed vertical wavelengths.

475 The weaker summer response of GW activity to geomagnetic disturbances may be
 476 due to a combination of seasonal variations in wave forcing, temperature structure and
 477 pre-existing GW activity. If Joule heating creates a portion of the observed GWs, the
 478 extent of Joule heating will be lesser in the enhanced ionospheric conductivities of the
 479 sunlit summer high latitudes compared to other seasons. The extent of particle heating
 480 in summer below 100 km is also lesser or of comparable magnitude to the other seasons
 481 - for example, compare Figure 4(j-l) with those of Figures 2(h), 5(h) and 6(h). These in-
 482 dicate that there is at least no excessive Joule or particle heating occurring in the sum-
 483 mer to force significantly larger amounts of GWs than other seasons.

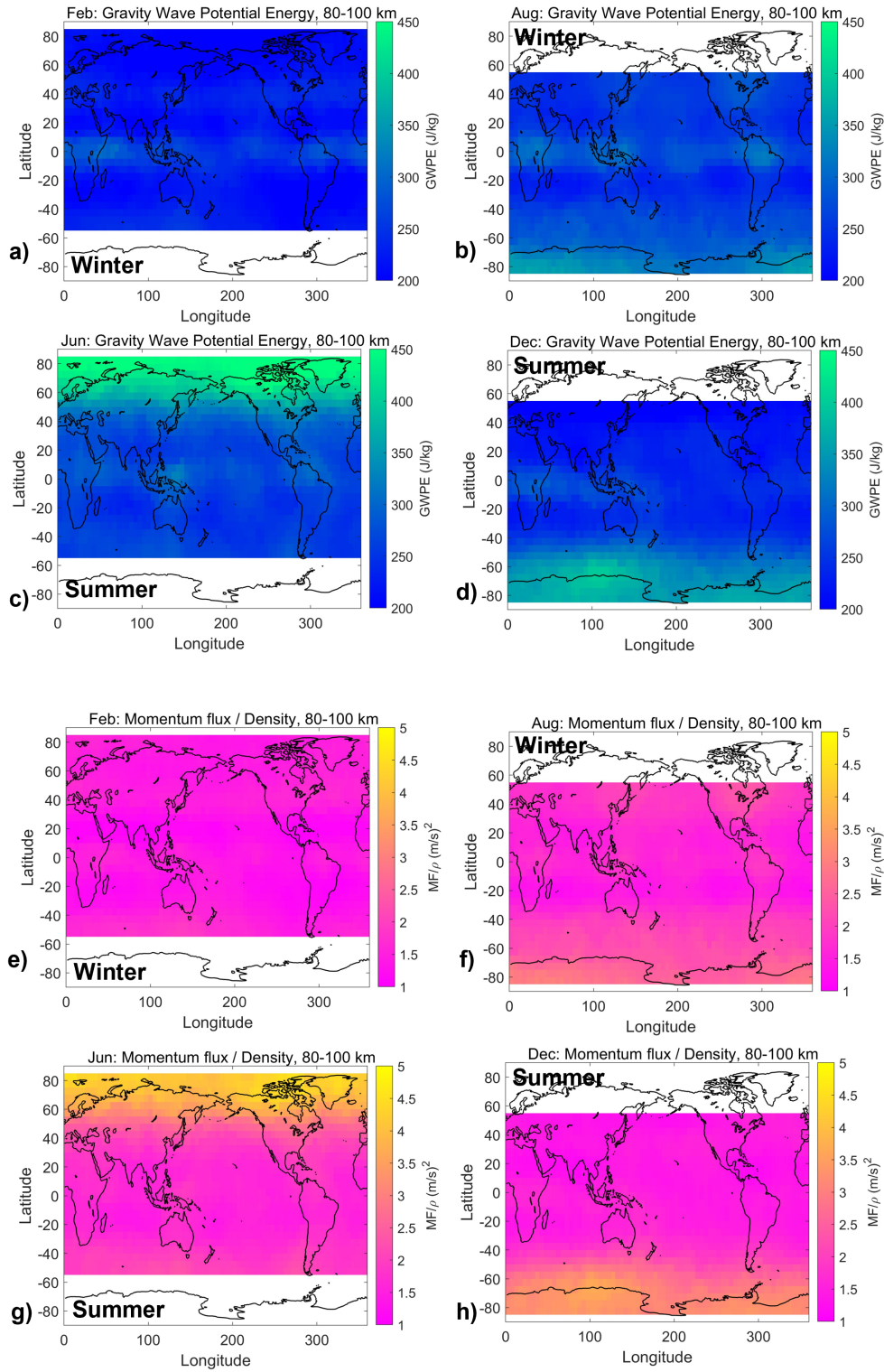


Figure 9. Climatology of GWPE (a-d) and MF/ρ (e-h). The left and right columns show Northern and Southern hemisphere climatologies, respectively. Winter season is given in (a,b,e and f) while summer in (c,d,g and h). Note, clear enhancements in the GW parameters in summer high latitudes and that the seasonal differences are largest in the Northern hemisphere.

484 Note that the upper mesospheric temperature structures in the high latitudes are
 485 broadly similar during the equinoxes and winter (for example, Figures 2(h), 5 and 6).
 486 The mesopause normally occur between 95 and 100 km in non-summer high latitude re-
 487 gion. However, during high latitude summer, it is well known that the mesopause de-
 488 scends to 85 - 90 km as seen in Figure 4(j-l). Therefore, in summer, the whole wave gen-
 489 eration region due to the auroral heating (both Joule and particle heating) lies in a steep
 490 lower thermospheric temperature gradient that could suppress the GWs.

491 Climatologies of GWPE and MF/ρ from SABER measurements between 2002 and
 492 2018 are shown in Figure 9. Panels (a-d) show GWPE and (e-h) show MF/ρ . The left
 493 (right) panels in the Figure show Northern (Southern) Hemispheric winter and summer
 494 seasons as alternating rows. Because of yaw changes of the TIMED satellite, coverage
 495 is poor at latitudes $> 55^\circ$ in one of the hemispheres even in the climatological averages
 496 and hence the variations are separately shown for the Northern and Southern Hemispheres.
 497 Two aspects can be clearly seen from the Figure: (i) wave activity in summer high lat-
 498 itudes are significantly higher in the altitude region of 80 - 100 km in both the hemispheres.
 499 Already existing strong wave activity during summer may reduce the contribution from
 500 geomagnetic activity compared to other seasons, resulting in a weaker summer response.
 501 (ii) the extent of the difference between winter and summer is greater in the Northern
 502 Hemisphere than the Southern Hemisphere (compare Figure 9(a and c) with (b and d)
 503 for GWPE and (e and g) with (f and h) for MF/ρ). Given that hemispheric asymmetries
 504 are an interesting contemporary research topic (Yan et al., 2021; Ern et al., 2022; Hong
 505 et al., 2023), the exact cause of such climatological differences needs further attention.

506 Also, the GW climatology during winter and equinoxes appears similar. We have
 507 not shown the climatologies for the equinoxes herein. Due to the yaw changes of SABER
 508 satellite, the data coverage for the climatologies for Autumn is better than those for spring.
 509 The Autumn climatologies for the month of October in the Northern hemisphere and
 510 for April in the Southern hemisphere closely resemble that of the winter climatologies
 511 in the respective hemispheres (i.e. Figure 9(a) and (e) are similar for climatology of Oc-
 512 tober and (b) and (f) for April). Therefore, the generation mechanisms, propagation con-
 513 ditions and pre-existing GW activity are broadly similar between the winter and equinoxes,
 514 while differing from that of summer both due to the temperature structure and due to
 515 large pre-existing GW activity.

516 Even during non-summer periods, the enhanced GW activity is seen only in 48%
 517 of cases. It is possible that chemical cooling effects due to nitric oxide may play a role
 518 in determining the GW response for a particular event. Improved upper-atmospheric mod-
 519 eling may aid understanding of the processes that lead to enhanced wave activity in some
 520 events and not in others. Moreover, a detailed study on the pattern of particle precip-
 521 itations and their relationship to observed GW enhancements might provide better in-
 522 sights on the interplay between wave generation and background conditions. It is rec-
 523 ognized that each geomagnetic event is different and the effects they produce are also
 524 largely variable. With the available information on temperatures up to 110 km, we are
 525 unable to experimentally establish the underlying cause for enhanced wave forcing in some
 526 events but not on some others, irrespective of seasons.

527 5 Summary and conclusion

528 This work shows for the first time the geographical regions and the altitudes from
 529 where the geomagnetic disturbances become an important GW source. We show that
 530 the geomagnetic activity generated GWs are dominant in the upper mesospheric region
 531 above 80 km in the high latitudes where particle precipitation along the magnetic field
 532 lines occur. The observed GW enhancements coincide with the duration of geomagnetic
 533 activity. No consistent GW enhancements are seen in the lower altitudes or latitudes be-
 534 low 55° . Noteworthy is the seasonality in the GW response to geomagnetic disturbances

535 wherein the summer hemisphere showed weakest response. This appears to be due to
 536 the lower mesopause altitude in summer along with a steep temperature gradient in the
 537 85 - 100 km region and larger pre-existing wave activity. We see a clear reduction in the
 538 mesopause height during non-summer periods owing to the heating by geomagnetic dis-
 539 turbance.

540 Nevertheless, the response in GW activity for geomagnetic disturbances is irreg-
 541 ular in all the seasons in that only 42% of the cases show an unambiguous increase in
 542 the GW activity. During non-summer periods, the percentage increases slightly to 48%.
 543 Therefore, in any particular case, there is no certainty in the enhancement of GW ac-
 544 tivity. This indicates that the pre-existing GWs excited by other lower atmospheric sources
 545 and background wind conditions combine with the forcing from geomagnetic activity in
 546 determining GW variability around a particular event. Detailed cases studies combin-
 547 ing both satellite and ground based measurements will help to gain a better understand-
 548 ing of reason behind some events not showing significant wave enhancements despite in-
 549 tense geomagnetic disturbances like that of 17 March 2015 superstorm.

551 6 Acknowledgements

552 The SABER/TIMED data used in this work can be obtained from [https://saber](https://saber.gats-inc.com/)
 553 [.gats-inc.com/](https://saber.gats-inc.com/), and AE and Dst indices from <https://wdc.kugi.kyoto-u.ac.jp/>.
 554 This work is supported by NERC project MesoS2D with grant numbers NE/V01837X/1,
 555 NE/V018426/1. CW is supported by Royal Society Fellowship URF\R\221023. NH is
 556 supported by NE/W003201/1 and NE/S00985X/1. PN is supported by a NERC GW4+
 557 Doctoral Training Partnership studentship NE/S007504/1.

558 References

- 559 Alexander, M. J., Gille, J., Cavanaugh, C., Coffey, M., Craig, C., Eden, T., ...
 560 Dean, V. (2008). Global estimates of gravity wave momentum flux from
 561 High Resolution Dynamics Limb Sounder observations. *Journal of Geo-*
 562 *physical Research: Atmospheres*, *113*(D15). Retrieved from [https://](https://agupubs.onlinelibrary.wiley.com/doi/abs/10.1029/2007JD008807)
 563 agupubs.onlinelibrary.wiley.com/doi/abs/10.1029/2007JD008807 doi:
 564 <https://doi.org/10.1029/2007JD008807>
- 565 Alken, P., Thébault, E., Beggan, C. D., Amit, H., Aubert, J., Baerenzung, J., ... et
 566 al. (2021). International geomagnetic reference field: The Thirteenth genera-
 567 tion. *Earth, Planets and Space*, *73*(1). doi: 10.1186/s40623-020-01288-x
- 568 Blanc, E., Ceranna, L., Hauchecorne, A., Charlton-Perez, A., Marchetti, E., Evers,
 569 L. G., ... et al. (2017). Toward an improved representation of middle atmo-
 570 spheric dynamics: thanks to the arise project. *Surveys in Geophysics*, *39*(2),
 571 171–225. doi: 10.1007/s10712-017-9444-0
- 572 Ern, M., Preusse, P., Alexander, M. J., & Warner, C. D. (2004). Absolute val-
 573 ues of gravity wave momentum flux derived from satellite data. *Journal of*
 574 *Geophysical Research: Atmospheres*, *109*(D20). Retrieved from [https://](https://agupubs.onlinelibrary.wiley.com/doi/abs/10.1029/2004JD004752)
 575 agupubs.onlinelibrary.wiley.com/doi/abs/10.1029/2004JD004752 doi:
 576 <https://doi.org/10.1029/2004JD004752>
- 577 Ern, M., Preusse, P., & Riese, M. (2022). Intermittency of gravity wave potential
 578 energies and absolute momentum fluxes derived from infrared limb sounding
 579 satellite observations. *Atmospheric Chemistry and Physics*, *22*(22), 15093–
 580 15133. Retrieved from [https://acp.copernicus.org/articles/22/15093/](https://acp.copernicus.org/articles/22/15093/2022/)
 581 [2022/](https://acp.copernicus.org/articles/22/15093/2022/) doi: 10.5194/acp-22-15093-2022
- 582 Esplin, R., Mlynczak, M. G., Russell, J., Gordley, L., & Team, T. S. (2023). Soun-
 583 ding of the Atmosphere using Broadband Emission Radiometry (SABER):

- Instrument and science measurement description. *Earth and Space Science*, 10, e2023EA002999. doi: <https://doi.org/10.1029/2023EA002999>
- Fleming, E. L., Chandra, S., Burrage, M. D., Skinner, W. R., Hays, P. B., Solheim, B. H., & Shepherd, G. G. (1996). Climatological mean wind observations from the UARS high-resolution Doppler imager and wind imaging interferometer: Comparison with current reference models. *Journal of Geophysical Research: Atmospheres*, 101(D6), 10455-10473. Retrieved from <https://agupubs.onlinelibrary.wiley.com/doi/abs/10.1029/95JD01043> doi: <https://doi.org/10.1029/95JD01043>
- Fritts, D. C., & Alexander, M. J. (2003). Gravity wave dynamics and effects in the middle atmosphere. *Reviews of Geophysics*, 41(1). Retrieved from <https://agupubs.onlinelibrary.wiley.com/doi/abs/10.1029/2001RG000106> doi: <https://doi.org/10.1029/2001RG000106>
- García-Comas, M., López-Puertas, M., Marshall, B. T., Wintersteiner, P. P., Funke, B., Bermejo-Pantaleón, D., ... Russell III, J. M. (2008). Errors in Sounding of the Atmosphere using Broadband Emission Radiometry (SABER) kinetic temperature caused by non-local-thermodynamic-equilibrium model parameters. *Journal of Geophysical Research: Atmospheres*, 113(D24). Retrieved from <https://agupubs.onlinelibrary.wiley.com/doi/abs/10.1029/2008JD010105> doi: <https://doi.org/10.1029/2008JD010105>
- Gottelman, A., Mills, M. J., Kinnison, D. E., Garcia, R. R., Smith, A. K., Marsh, D. R., ... Randel, W. J. (2019). The Whole Atmosphere Community Climate Model Version 6 (WACCM6). *Journal of Geophysical Research: Atmospheres*, 124(23), 12380-12403. Retrieved from <https://agupubs.onlinelibrary.wiley.com/doi/abs/10.1029/2019JD030943> doi: <https://doi.org/10.1029/2019JD030943>
- Gordley, L. L., Hervig, M. E., Fish, C., Russell, J. M., Bailey, S., Cook, J., ... Kemp, J. (2009). The solar occultation for ice experiment. *Journal of Atmospheric and Solar-Terrestrial Physics*, 71(3), 300-315. Retrieved from <https://www.sciencedirect.com/science/article/pii/S136468260800206X> (Global Perspectives on the Aeronomy of the Summer Mesopause Region) doi: <https://doi.org/10.1016/j.jastp.2008.07.012>
- Harding, B. J., Makela, J. J., Englert, C. R., Marr, K. D., Harlander, J. M., England, S. L., & Immel, T. J. (2017). The MIGHTI wind retrieval algorithm: Description and verification. *Space Science Reviews*, 212(1-2), 585-600. doi: [10.1007/s11214-017-0359-3](https://doi.org/10.1007/s11214-017-0359-3)
- Harvey, V. L., Pedatella, N., Becker, E., & Randall, C. (2022). Evaluation of Polar Winter Mesopause Wind in WACCMX+DART. *Journal of Geophysical Research: Atmospheres*, 127(15), e2022JD037063. Retrieved from <https://agupubs.onlinelibrary.wiley.com/doi/abs/10.1029/2022JD037063> doi: <https://doi.org/10.1029/2022JD037063>
- Hertzog, A., Alexander, M. J., & Plougonven, R. (2012). On the intermittency of gravity wave momentum flux in the stratosphere. *Journal of the Atmospheric Sciences*, 69(11), 3433 - 3448. Retrieved from <https://journals.ametsoc.org/view/journals/atsc/69/11/jas-d-12-09.1.xml> doi: <https://doi.org/10.1175/JAS-D-12-09.1>
- Hindley, N. P., Mitchell, N. J., Cobbett, N., Smith, A. K., Fritts, D. C., Janches, D., ... Moffat-Griffin, T. (2022). Radar observations of winds, waves and tides in the mesosphere and lower thermosphere over South Georgia island (54 S, 36 W) and comparison with WACCM simulations. *Atmospheric Chemistry and Physics*, 22(14), 9435-9459. Retrieved from <https://acp.copernicus.org/articles/22/9435/2022/> doi: [10.5194/acp-22-9435-2022](https://doi.org/10.5194/acp-22-9435-2022)
- Hindley, N. P., Wright, C. J., Smith, N. D., Hoffmann, L., Holt, L. A., Alexander, M. J., ... Mitchell, N. J. (2019). Gravity waves in the winter stratosphere over the southern ocean: high-resolution satellite observations and 3-d spectral

- 639 analysis. *Atmospheric Chemistry and Physics*, 19(24), 15377–15414. Re-
 640 trieved from <https://acp.copernicus.org/articles/19/15377/2019/> doi:
 641 10.5194/acp-19-15377-2019
- 642 Hong, Y., Deng, Y., Zhu, Q., Maute, A., Hairston, M. R., Waters, C., ... Lopez,
 643 R. E. (2023). Inter-hemispheric asymmetries in high-latitude electrodynamic
 644 forcing and the thermosphere during the October 8-9, 2012, geomagnetic
 645 storm: An integrated data -model investigation. *Frontiers in Astronomy
 646 and Space Sciences*, 10. Retrieved from [https://www.frontiersin.org/
 647 articles/10.3389/fspas.2023.1062265](https://www.frontiersin.org/articles/10.3389/fspas.2023.1062265) doi: 10.3389/fspas.2023.1062265
- 648 Hunsucker, R. D. (1982). Atmospheric gravity waves generated in the high-latitude
 649 ionosphere: A review. *Reviews of Geophysics*, 20(2), 293-315. Retrieved
 650 from [https://agupubs.onlinelibrary.wiley.com/doi/abs/10.1029/
 651 RG020i002p00293](https://agupubs.onlinelibrary.wiley.com/doi/abs/10.1029/RG020i002p00293) doi: <https://doi.org/10.1029/RG020i002p00293>
- 652 Jin, H., Miyoshi, Y., Fujiwara, H., Shinagawa, H., Terada, K., Terada, N., ... Saito,
 653 A. (2011). Vertical connection from the tropospheric activities to the iono-
 654 spheric longitudinal structure simulated by a new Earth's whole atmosphere-
 655 ionosphere coupled model. *Journal of Geophysical Research: Space Physics*,
 656 116(A1). Retrieved from [https://agupubs.onlinelibrary.wiley.com/doi/
 657 abs/10.1029/2010JA015925](https://agupubs.onlinelibrary.wiley.com/doi/abs/10.1029/2010JA015925) doi: <https://doi.org/10.1029/2010JA015925>
- 658 John, S. R., & Kumar, K. K. (2012). TIMED/SABER observations of global grav-
 659 ity wave climatology and their interannual variability from stratosphere to
 660 mesosphere lower thermosphere. *Climate Dynamics*, 39(6), 1489-1505. doi:
 661 10.1007/s00382-012-1329-9
- 662 McDonald, A. J. (2012). Gravity wave occurrence statistics derived from paired
 663 COSMIC/FORMOSAT3 observations. *Journal of Geophysical Research: At-
 664 mospheres*, 117(D15). Retrieved from [https://agupubs.onlinelibrary
 665 .wiley.com/doi/abs/10.1029/2011JD016715](https://agupubs.onlinelibrary.wiley.com/doi/abs/10.1029/2011JD016715) doi: [https://doi.org/10.1029/
 666 2011JD016715](https://doi.org/10.1029/2011JD016715)
- 667 McLandress, C., Shepherd, G. G., Solheim, B. H., Burrage, M. D., Hays, P. B.,
 668 & Skinner, W. R. (1996). Combined mesosphere/thermosphere winds us-
 669 ing WINDII and HRDI data from the Upper Atmosphere Research Satel-
 670 lite. *Journal of Geophysical Research: Atmospheres*, 101(D6), 10441-10453.
 671 Retrieved from [https://agupubs.onlinelibrary.wiley.com/doi/abs/
 672 10.1029/95JD01706](https://agupubs.onlinelibrary.wiley.com/doi/abs/10.1029/95JD01706) doi: <https://doi.org/10.1029/95JD01706>
- 673 Mertens, C. J., Russell III, J. M., Mlynczak, M. G., She, C.-Y., Schmidlin, F. J.,
 674 Goldberg, R. A., ... Xu, X. (2009). Kinetic temperature and carbon diox-
 675 ide from broadband infrared limb emission measurements taken from the
 676 TIMED/SABER instrument. *Advances in Space Research*, 43(1), 15-27.
 677 Retrieved from [https://www.sciencedirect.com/science/article/pii/
 678 S0273117708002883](https://www.sciencedirect.com/science/article/pii/S0273117708002883) doi: <https://doi.org/10.1016/j.asr.2008.04.017>
- 679 Narayanan, V. L., Gurubaran, S., & Emperumal, K. (2012). Nightglow imag-
 680 ing of different types of events, including a mesospheric bore observed on
 681 the night of February 15, 2007 from Tirunelveli (8.7 N). *Journal of Atmo-
 682 spheric and Solar-Terrestrial Physics*, 78-79, 70-83. Retrieved from [https://
 683 www.sciencedirect.com/science/article/pii/S136468261100215X](https://www.sciencedirect.com/science/article/pii/S136468261100215X) doi:
 684 <https://doi.org/10.1016/j.jastp.2011.07.006>
- 685 Noble, P., Hindley, N., Wright, C., Cullens, C., England, S., Pedatella, N., ...
 686 Moffat-Griffin, T. (2022). Interannual variability of winds in the antarctic
 687 mesosphere and lower thermosphere over rothera (67°S, 68°W) in radar
 688 observations and waccm-x. *Atmospheric Chemistry and Physics Discussions*,
 689 2022, 1–29. Retrieved from [https://acp.copernicus.org/preprints/
 690 acp-2022-150/](https://acp.copernicus.org/preprints/acp-2022-150/) doi: 10.5194/acp-2022-150
- 691 Oyama, S., & Watkins, B. J. (2012). Generation of Atmospheric Gravity Waves
 692 in the Polar Thermosphere in Response to Auroral Activity. *Space Science Re-
 693 views*, 168, 463-473. doi: 10.1007/s11214-011-9847-z

- 694 Ramkumar, T., Gurubaran, S., & Rajaram, R. (2002). Lower E-region MF radar
695 spaced antenna measurements over magnetic equator. *Journal of Atmospheric*
696 *and Solar-Terrestrial Physics*, *64*(12), 1445-1453. Retrieved from [https://](https://www.sciencedirect.com/science/article/pii/S1364682602001086)
697 www.sciencedirect.com/science/article/pii/S1364682602001086 doi:
698 [https://doi.org/10.1016/S1364-6826\(02\)00108-6](https://doi.org/10.1016/S1364-6826(02)00108-6)
- 699 Reid, I. M. (2015). MF and HF radar techniques for investigating the dynamics and
700 structure of the 50 to 110 km height region: a review. *Progress in Earth and*
701 *Planetary Science*, *2*, 33. doi: 10.1186/s40645-015-0060-7
- 702 Remsberg, E. E., Marshall, B. T., Garcia-Comas, M., Krueger, D., Lingenfelter,
703 G. S., Martin-Torres, J., ... Thompson, R. E. (2008). Assessment of the qual-
704 ity of the Version 1.07 temperature-versus-pressure profiles of the middle atmo-
705 sphere from TIMED/SABER. *Journal of Geophysical Research: Atmospheres*,
706 *113*(D17). Retrieved from [https://agupubs.onlinelibrary.wiley.com/doi/](https://agupubs.onlinelibrary.wiley.com/doi/abs/10.1029/2008JD010013)
707 [abs/10.1029/2008JD010013](https://agupubs.onlinelibrary.wiley.com/doi/abs/10.1029/2008JD010013) doi: <https://doi.org/10.1029/2008JD010013>
- 708 Roble, R. G., & Ridley, E. C. (1994). A thermosphere-ionosphere-mesosphere-
709 electrodynamics general circulation model (Time-GCM): Equinox solar cycle
710 minimum simulations (30–500 km). *Geophysical Research Letters*, *21*(6), 417-
711 420. Retrieved from [https://agupubs.onlinelibrary.wiley.com/doi/abs/](https://agupubs.onlinelibrary.wiley.com/doi/abs/10.1029/93GL03391)
712 [10.1029/93GL03391](https://agupubs.onlinelibrary.wiley.com/doi/abs/10.1029/93GL03391) doi: <https://doi.org/10.1029/93GL03391>
- 713 Shepherd, G. G., Thuillier, G., Cho, Y.-M., Duboin, M.-L., Evans, W. F. J.,
714 Gault, W. A., ... Ward, W. E. (2012). The Wind Imaging Interferom-
715 eter (WINDII) on the Upper Atmosphere Research Satellite: A 20 year
716 perspective. *Reviews of Geophysics*, *50*(2). Retrieved from [https://](https://agupubs.onlinelibrary.wiley.com/doi/abs/10.1029/2012RG000390)
717 agupubs.onlinelibrary.wiley.com/doi/abs/10.1029/2012RG000390 doi:
718 <https://doi.org/10.1029/2012RG000390>
- 719 Siskind, D. E., Jones Jr., M., Drob, D. P., McCormack, J. P., Hervig, M. E., Marsh,
720 D. R., ... Mitchell, N. J. (2019). On the relative roles of dynamics and
721 chemistry governing the abundance and diurnal variation of low-latitude
722 thermospheric nitric oxide. *Annales Geophysicae*, *37*(1), 37–48. Retrieved
723 from <https://angeo.copernicus.org/articles/37/37/2019/> doi:
724 [10.5194/angeo-37-37-2019](https://doi.org/10.5194/angeo-37-37-2019)
- 725 Smith, A. K. (2012). Global Dynamics of the MLT. *Surveys in Geophysics*, *33*(6),
726 1177–1230. doi: 10.1007/s10712-012-9196-9
- 727 Smith, A. K., Pedatella, N. M., Marsh, D. R., & Matsuo, T. (2017). On the Dy-
728 namical Control of the Mesosphere - Lower Thermosphere by the Lower and
729 Middle Atmosphere. *Journal of the Atmospheric Sciences*, *74*(3), 933 - 947.
730 Retrieved from [https://journals.ametsoc.org/view/journals/atsc/74/3/](https://journals.ametsoc.org/view/journals/atsc/74/3/jas-d-16-0226.1.xml)
731 [jas-d-16-0226.1.xml](https://journals.ametsoc.org/view/journals/atsc/74/3/jas-d-16-0226.1.xml) doi: <https://doi.org/10.1175/JAS-D-16-0226.1>
- 732 Stober, G., Kuchar, A., Pokhotelov, D., Liu, H., Liu, H.-L., Schmidt, H., ...
733 Mitchell, N. (2021). Interhemispheric differences of mesosphere-lower ther-
734 mosphere winds and tides investigated from three whole-atmosphere models
735 and meteor radar observations. *Atmospheric Chemistry and Physics*, *21*(18),
736 13855–13902. Retrieved from [https://acp.copernicus.org/articles/21/](https://acp.copernicus.org/articles/21/13855/2021/)
737 [13855/2021/](https://acp.copernicus.org/articles/21/13855/2021/) doi: 10.5194/acp-21-13855-2021
- 738 Stockwell, R., Mansinha, L., & Lowe, R. (1996). Localization of the complex spec-
739 trum: the S transform. *IEEE Transactions on Signal Processing*, *44*(4), 998-
740 1001. doi: 10.1109/78.492555
- 741 Wright, C. J., & Gille, J. C. (2013). Detecting overlapping gravity waves using the
742 S-Transform. *Geophysical Research Letters*, *40*(9), 1850-1855. Retrieved from
743 <https://agupubs.onlinelibrary.wiley.com/doi/abs/10.1002/grl.50378>
744 doi: <https://doi.org/10.1002/grl.50378>
- 745 Wright, C. J., Hindley, N. P., Moss, A. C., & Mitchell, N. J. (2016). Multi-
746 instrument gravity-wave measurements over Tierra del Fuego and the Drake
747 Passage - Part 1: Potential energies and vertical wavelengths from AIRS,
748 COSMIC, HIRDLS, MLS-Aura, SAAMER, SABER and radiosondes. *Atmo-*

- 749 *spheric Measurement Techniques*, 9(3), 877–908. Retrieved from [https://](https://amt.copernicus.org/articles/9/877/2016/)
750 amt.copernicus.org/articles/9/877/2016/ doi: 10.5194/amt-9-877-2016
- 751 Wright, C. J., Rivas, M. B., & Gille, J. C. (2011). Intercomparisons of HIRDLS,
752 COSMIC and SABER for the detection of stratospheric gravity waves. *At-*
753 *mospheric Measurement Techniques*, 4(8), 1581–1591. Retrieved from
754 <https://amt.copernicus.org/articles/4/1581/2011/> doi: 10.5194/
755 amt-4-1581-2011
- 756 Wu, C., & Ridley, A. J. (2023). Comparison of TIDI line of sight winds with ICON-
757 MIGHTI measurements. *Journal of Geophysical Research: Space Physics*,
758 128(2), e2022JA030910. Retrieved from [https://agupubs.onlinelibrary](https://agupubs.onlinelibrary.wiley.com/doi/abs/10.1029/2022JA030910)
759 [.wiley.com/doi/abs/10.1029/2022JA030910](https://agupubs.onlinelibrary.wiley.com/doi/abs/10.1029/2022JA030910) doi: [https://doi.org/10.1029/](https://doi.org/10.1029/2022JA030910)
760 2022JA030910
- 761 Yan, X., Konopka, P., Hauck, M., Podglajen, A., & Ploeger, F. (2021). Asymmetry
762 and pathways of inter-hemispheric transport in the upper troposphere and
763 lower stratosphere. *Atmospheric Chemistry and Physics*, 21(9), 6627–6645.
764 Retrieved from <https://acp.copernicus.org/articles/21/6627/2021/>
765 doi: 10.5194/acp-21-6627-2021
- 766 Zawdie, K., Belehaki, A., Burleigh, M., Chou, M.-Y., Dhadly, M. S., Greer, K., ...
767 Zhang, S.-R. (2022). Impacts of acoustic and gravity waves on the iono-
768 sphere. *Frontiers in Astronomy and Space Sciences*, 9. Retrieved from
769 <https://www.frontiersin.org/articles/10.3389/fspas.2022.1064152>
770 doi: 10.3389/fspas.2022.1064152